Monthly Notices
of the
ROYAL ASTRONOMICAL SOCIETY

MNRAS **447,** 1033–1048 (2015) doi:10.1093/mnras/stu2480

Radial variations in the stellar initial mass function of early-type galaxies

Ignacio Martín-Navarro,[1,2]★ Francesco La Barbera,[3] Alexandre Vazdekis,[1,2] Jesús Falcón-Barroso[1,2] and Ignacio Ferreras[4]

[1]*Instituto de Astrofísica de Canarias, E-38200 La Laguna, Tenerife, Spain*
[2]*Departamento de Astrofísica, Universidad de La Laguna, E-38205 La Laguna, Tenerife, Spain*
[3]*INAF–Osservatorio Astronomico di Capodimonte, Napoli, Italy*
[4]*Mullard Space Science Laboratory, University College London, Holmbury St Mary, Dorking, Surrey RH5 6NT, UK*

Accepted 2014 November 22. Received 2014 November 4; in original form 2014 April 23

ABSTRACT

The hypothesis of a universal initial mass function (IMF) – motivated by observations in nearby stellar systems – has been recently challenged by the discovery of a systematic variation of the IMF with the central velocity dispersion, σ, of early-type galaxies (ETGs), towards an excess of low-mass stars in high-σ galaxies. This trend has been derived so far from integrated spectra, and remains unexplained at present. To test whether such trend depends on the *local* properties within a galaxy, we have obtained new, extremely deep, spectroscopic data, for three nearby ETGs, two galaxies with high σ ($\sim$300 km s^{-1}), and one lower mass system, with $\sigma \sim 100$ km s^{-1}. From the analysis of IMF-sensitive spectral features, we find that the IMF depends significantly on galactocentric distance in the massive ETGs, with the enhanced fraction of low-mass stars mostly confined to their central regions. In contrast, the low-σ galaxy does not show any significant radial gradient in the IMF, well described by a shallower distribution, relative to the innermost regions of massive galaxies, at all radii. Such a result indicates that the IMF should be regarded as a local (rather than global) property, and suggests a significant difference between the formation process of the core and the outer regions of massive ETGs.

Key words: galaxies: elliptical and lenticular, cD – galaxies: evolution – galaxies: formation – galaxies: fundamental parameters.

1 INTRODUCTION

The stellar initial mass function (IMF) characterizes the distribution of stellar masses at birth in star-forming regions. The IMF is therefore a crucial ingredient of galaxy formation and evolution. It sets the mass scale of galaxies, determining their (stellar) mass-to-light ratio, and drives stellar feedback as well as chemical enrichment into the interstellar medium (ISM). While resolved stellar population studies support the idea of an invariant IMF in environments with quite different local properties such as metallicity or density (Kroupa 2002; Bastian, Covey & Meyer 2010; Kroupa et al. 2013), recent studies of early-type galaxies (ETGs), based on both dynamics (Thomas et al. 2011; Cappellari et al. 2012; Wegner et al. 2012; Dutton et al. 2013; Tortora et al. 2013) and stellar populations (Saglia et al. 2002; Cenarro et al. 2003; van Dokkum & Conroy 2010; Spiniello et al. 2012; Ferreras et al. 2013; La Barbera et al. 2013) have found that the IMF varies with galaxy mass. The same result has also been obtained by a combination of gravitational lensing and dynamical studies (Auger et al. 2010; Treu et al. 2010, but also see Smith & Lucey 2013). In particular, dynamical studies have found a significant increase of the stellar mass-to-light ratio, with respect to that expected for a 'standard', Milky Way-like IMF, towards high-mass systems. The analysis of gravity-sensitive features in the integrated spectra of ETGs has revealed that this trend in the 'normalization' of the IMF is driven by an increase of the fraction of dwarf-to-giant stars, i.e. a change towards steeper IMF slopes with higher velocity dispersion (Cenarro et al. 2003; Falcón-Barroso et al. 2003; Cappellari et al. 2012; Ferreras et al. 2013; La Barbera et al. 2013, hereafter LB13). Although some discrepancies can be found between dynamical and stellar population studies, the agreement is remarkable, considering the fundamental differences of both approaches (Smith 2014).

One should notice that the results from stellar population studies are derived from integrated spectra, therefore correspond mostly to the bright central regions of ETGs. Therefore, the question of whether radial variations *within* a galaxy occur, follows naturally. Are these variations in the IMF driven by a large-scale (e.g. galaxy mass) or a local property (e.g. local velocity dispersion)? Despite the importance of this question to constrain the overall picture of galaxy formation and evolution, no reliable spatially resolved measurement of the IMF has been performed so far. Only a few early attempts tried

★E-mail: imartin@iac.es

to investigate this issue. Carter, Visvanathan & Pickles (1986) found strong radial gradients of Na and TiO spectral features in ETGs, interpreting it as the contribution from metal-rich populations of dwarf stars, concentrated towards the centres of the most massive galaxies. This interpretation was dismissed by Cohen (1979), Hardy & Couture (1988) and Delisle & Hardy (1992), who suggested instead metallicity alone as the driver of these radial trends. Due to the lack of accurate stellar population models and high-quality data at the time, these pioneering attempts remained inconclusive.

Over 20 years later, in this work, we show that after considerable improvement in the state-of-the-art stellar population synthesis models, analysis tools, observational facilities, and instrumentation, we are now able to address the issue of a radial variation of the IMF in unresolved stellar populations. Targeting a set of optical and near-infrared (NIR) gravity-sensitive spectral features in two high-σ ($\sim$300 km s^{-1}) and one low-σ ($\sim$100 km s^{-1}) ETGs, we find that variations in the IMF of these systems should be regarded as a local property.

The outline of the paper is the following. In Section 2, we describe the sample of ETGs and data reduction. Section 3 presents the stellar population analysis. Section 4 shows the main results of this work, i.e. the IMF trend as a function of galactocentric distance in ETGs. In Section 5, we present results from a number of tests performed to assess the robustness of our results. In Section 6, we discuss several effects that might mimic an IMF gradient, showing that none of them can account for all the available data. Our results are discussed in Section 7, and conclusions are given in Section 8. Further material is presented in Appendix B, to address possible technical issues of the stellar population analysis.

2 SAMPLE AND DATA REDUCTION

We obtained deep spectroscopic data of three nearby ETGs, with different masses and different radial profiles of velocity dispersion. NGC 4552 and NGC 5557 are massive ETGs, with a velocity dispersion σ $\sim$300 km s^{-1} in their centre (Emsellem et al. 2011), whereas NGC 4387 is a lower mass system with a central value of σ $\sim$ 100 km s^{-1}. The effective radii are, 18.85, 36.31 and 28.84 arcsec for NGC 4387, NGC 4552 and NGC 5557, respectively (Cappellari et al. 2011). Because the spectra of NGC 5557 turned out to be significantly affected by telluric absorption, we analysed its data following a different approach than for NGC 4552 and NGC 4387. While the kinematics of NGC 5557 is presented in Section 3.1, together with that for the other two galaxies, the analysis of the IMF is presented separately, in Appendix A. Throughout the paper, we refer to NGC 4387 and NGC 4552 as our reference low- and high-mass ETGs. We notice that both NGC 4387 and NGC 4552 (as well as NGC 5557) are not peculiar in terms of either kinematics or stellar population properties (Cappellari et al. 2011).

The observations were carried out at the 10.4 m Gran Telescopio Canarias, with the OSIRIS (Cepa et al. 2000) spectrograph. The spectra cover the range from 4500 to 10 000 Å with a resolution of R = 2500 for λ < 6000 Å, and R = 1000 otherwise. The slit used has 1.0 arcsec × 7.8 arcmin along the spectral and spatial directions, respectively. The wide wavelength range allows us to target IMF-sensitive absorption features that are sensitive to different chemical species (mostly, Na, Ca, and Ti). This is crucial to distinguish between the effect of a varying IMF and other effects possibly affecting gravity-sensitive indices, such as variations of elemental abundance ratios. Each target was observed for 1.5 h, allowing us to achieve the high signal-to-noise ratio (S/N) required to analyse the IMF effect on absorption features.

Data reduction was done with the REDUCEME package (Cardiel 1999), allowing for a careful propagation of different sources of uncertainties during the reduction. This is crucial for our purposes, as we aim to explore different galactocentric regions – up to about one effective radius – where systematic effects might be potentially important because of the low surface brightness level. We performed the usual spectroscopic reduction steps, including bias subtraction, flat-fielding, cosmic ray cleaning, sky subtraction, C-distortion correction, wavelength calibration (better than $\Delta\lambda$ $\sim$ 8 per cent), S-distortion correction, extinction correction and flux calibration.

In order to measure the radial variation of the IMF, for each galaxy we produced averaged spectra in different radial bins. To this effect, we first corrected, line-by-line, the 2D reduced spectrum to the rest frame (removing both systemic and rotation velocity), and convolved each spectrum (i.e. each line) to match the maximum velocity dispersion of the galaxy (see Section 3.1 for details on the determination of the kinematics). Then, we defined radial bins adaptively, summing up the spectra along the slit position incrementally, until a target S/N $\geq$100 Å^{-1} was reached for each bin.

3 ANALYSIS

3.1 Kinematics

To measure the radial velocity and velocity dispersion profiles, we used the software PPXF (Cappellari & Emsellem 2004). The S/N requirement for the measurement of the kinematics is lower than for the analysis of the stellar populations. Thus, as explained above, we corrected the differences in the kinematics of individual spectra within the radial bins to be used in the study of the stellar population properties. In Fig. 1, we show the profiles of velocity dispersion and radial velocity as a function of normalized galactocentric distance, $R/R_{\rm e}$, for all three galaxies observed with GTC-OSIRIS. Our measurements are in agreement with previous results (Emsellem et al. 2011), with the massive galaxy NGC 4552, as well as the additional high-mass system NGC 5557 (Appendix A), being slow rotators ($\lambda_{\rm Re}$ = 0.049 for both galaxies), and the low-mass galaxy NGC 4387 classified as a fast rotator ($\lambda_{\rm Re}$ = 0.399).

3.2 Stellar population models

We analysed the spectra of each galaxy, at each galactocentric distance, with the Vazdekis et al. (2012) extended version of MILES stellar population models (Vazdekis et al. 2010), hereafter defined as MIUSCAT models. These models combine a variety of empirical stellar libraries over the spectral range λλ3465–9469 Å, at a nominal resolution of 2.51 Å full width at half-maximum, relying on solar-scaled isochrones with stellar spectra following the abundance pattern of our Galaxy, i.e. approximately solar scaled at solar metallicity. We consider a variety of extended MILES simple stellar population (SSP) models covering a wide range of ages, from 0.5 to 14 Gyr, and metallicities, from [Z/H] = −0.4 to +0.3, as well as different IMF slopes. Notice that we did not use SSPs younger than 0.5 Gyr and with [Z/H] < −0.4, as our targeted ETGs are mostly composed of old, metal-rich, stellar populations. For metallicities above +0.22 – the maximum MILES value – SSPs are computed by linear extrapolation of the available models. However, our conclusions are not affected at all by this extrapolation, as only the innermost radial bin of NGC 4552 benefits from it (see Section 4.2). For the present study, we consider the bimodal IMF (Vazdekis et al. 1996), consisting of a power law at high masses, with index $\Gamma_{\rm b}$, tapered off to a constant value at M < 0.6 M$_{\odot}$. As shown in our

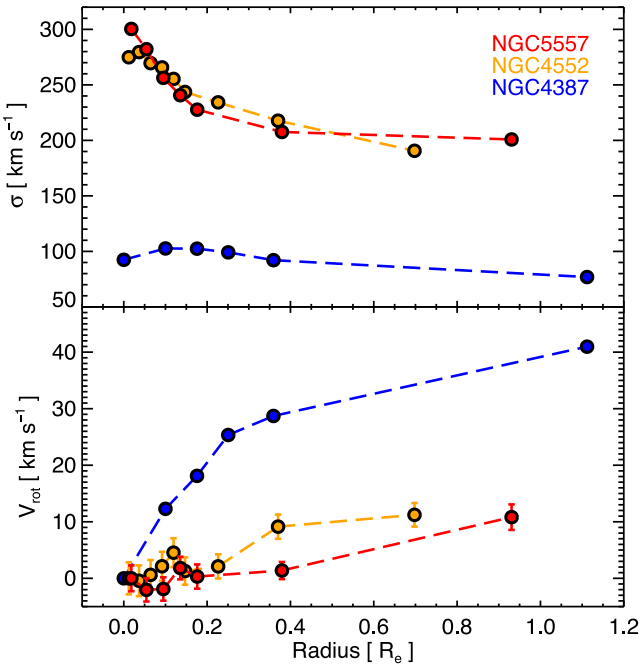

Figure 1. Radial gradients of velocity dispersion (top) and rotation velocity (bottom), from our GTC-OSIRIS observations, i.e. for NGC 4552, NGC 4387, and the additional massive galaxy NGC 5557. The profiles are plotted against the normalized galactocentric distance, R/R_e. The two massive galaxies, NGC 5557 and NGC 4552, show a decreasing σ profile, while the low-mass system, NGC 4387, has an almost constant velocity dispersion profile. Error bars in σ are smaller than the symbol size. Notice that the radial velocity is more important in the fast rotator NGC 4387 than in the two massive slow rotators (NGC 4552 and NGC 5557). The increasing distance of radial bins reflects the S/N criterion imposed to perform an adaptive binning of the available spectra along the slit spatial direction.

previous work (LB13), both bimodal and unimodal – i.e. single-segment, Salpeter-like IMFs (Salpeter 1955) – are able to describe equally well the gravity-sensitive features of ETGs, but bimodal IMFs provide mass-to-light ratios in better agreement with dynamical constraints. For $\Gamma_b \sim 1.35$, the bimodal IMF represents well the canonical, Kroupa-like IMF (e.g. Kroupa 2001). Lower (higher) values of Γ_b correspond to top- (bottom-) heavy distributions, with an excess of high- (low-) mass stars. The lower and upper mass cutoffs of the IMFs are set to 0.1 and 100 $M_\odot$, respectively, while the IMF slope, Γ_b, is allowed to vary from $\Gamma_b = 0.3$ to 3.3, where MILES models provide robust predictions (Vazdekis et al. 2012).

3.3 Fitting process

For each spectrum, i.e. each galaxy and radial bin, we infer the best-fitting slope of the bimodal IMF, Γ_b, by minimizing the expression:

$$\chi^2(\Gamma_b, [Z/H], \delta Ti) = \left[\frac{Age(\Gamma_b) - Age_M}{\sigma_{Age}}\right]^2 + \sum_i \left[\frac{(EW_i - C_{\alpha,i}\cdot[\alpha/Fe] - \Delta_{Ti,i}\cdot\delta Ti) - EW_{M,i}}{\sigma_{EW_i}}\right]^2, \quad (1)$$

where $Age(\Gamma_b)$ is the (Γ_b-dependent) estimate of the age, obtained from spectral fitting (see Section 3.3.2 for details); EW_i are the measured equivalent widths (i.e. line strengths) for a selected set of spectral features (see Section 3.3.1); and Age_M and $EW_{M,i}$ are the Age and equivalent widths of (MILES) SSP models; $C_{\alpha,i}$ is the observed sensitivity of the ith index to [α/Fe] (see Section 3.3.3); $\Delta_{Ti,i}$ is the expected sensitivity (from Conroy & van Dokkum 2012, hereafter CvD12, theoretical stellar population models) to [Ti/Fe] abundance, and δTi is a 'residual' TiO-based abundance correction[1] (i.e. not accounted for by the $C_{\alpha,i}$ terms; see LB13). The χ^2 minimization is performed over a range of SSP models, with varying age, metallicity, and IMF (see Section 3.2). The σ_{Age} is a re-scaled uncertainty on $Age(\Gamma_b)$, defined by dividing the 1σ error on age (σ'_{Age}, as estimated from spectral fitting, see Section 3.3.2 below) by the root square of the number of indices used in the fitting. In practise, this procedure ensures that the age of the SSP model that minimizes the χ^2 (equation 1) is always close to the age estimate from spectral fitting, i.e. that the age of the preferred SSP model is *not* driven by the IMF-sensitive features (e.g. TiO_1, TiO_2, and Mg4780, whose sensitivity to age, in addition to IMF slope, is also significant; see Section 3.3.1).

The free-fitting parameters are therefore IMF slope (Γ_b); total metallicity ([Z/H]); and a Ti-related correction (δTi), whereas age is a constrained fitting parameter (its value being constrained, within σ_{Age}, to the estimate obtained from spectral fitting, for each Γ_b). Uncertainties on best-fitting parameters are estimated by shifting the EW_i's and $Age(\Gamma_b)$ (see equation 1) according to their errors (σ_{EW_i} and σ'_{Age}, respectively), and repeating the χ^2 minimization procedure. The uncertainty of a given parameter is bootstrapped from the standard deviation of best-fitting repeated estimates. The term $C_{\alpha,i}\cdot$[α/Fe] corrects the observed line strengths to [α/Fe]=0, allowing a more direct comparison to the reference, solar-scaled, MILES models. The term $\Delta_{Ti,i}\cdot\delta$Ti removes the effect of residual [Ti/Fe] abundance (and flux calibration effects, see details in Section 5) from line strengths. The crucial aspects of equation (1), and the rationale beyond all different terms in it, are explained in the following subsections (Section 3.3). We remark that for NGC 5557, because of significant contamination from telluric absorption in the spectra, we have analysed the spectra separately, with a different set of indices, as detailed in Appendix A.

3.3.1 *Spectral indices*

The spectral features we use in the χ^2 minimization procedure include the total metallicity indicator [MgFe]$'$ (Thomas, Maraston & Bender 2003), and the following set of gravity-sensitive features: Mg 4780 (Serven, Worthey & Briley 2005), TiO_1 (Trager et al. 1998) ($\lambda \sim 5960$ Å), TiO_2 (Trager et al. 1998) ($\lambda \sim 6230$ Å), and Ca_2 (Cenarro et al. 2001) ($\lambda \sim 8540$ Å), all of them showing a significant response to a varying fraction of low- to high-mass stars in the IMF (LB13). We note that other (gravity-sensitive) NIR calcium absorption lines, Ca_1 ($\lambda \sim 8500$ Å) and Ca_3 ($\lambda \sim 8660$ Å), entering the definition of the calcium triplet (CaT≡Ca_1 +Ca_2 +Ca_3; see Cenarro et al. 2001), are severely contaminated by airglow in the spectra of our sample of ETGs, and thus are not considered in this paper. Other well-known gravity-sensitive features, including the optical Na doublet NaD ($\lambda \sim 5900$ Å), and the NIR Na I doublet feature (Schiavon, Barbuy & Bruzual 2000) Na I 8190 ($\lambda\lambda$ 8183,8195 Å), are also contaminated by airglow and telluric absorption. However, as shown in Appendix B, the contamination mostly affects the absolute value of the indices, while their radial variation (i.e. the gradient) is robust. Therefore, while we do not

[1] Notice, also, that δTi *is not* a Titanium abundance measurement ([Ti/Fe]), since δTi strongly depends on flux calibration at the level of a few per cent (see Section 5 and Appendix C).

include Na features in the χ^2 minimization procedure, we compare their observed gradients to model gradients, accounting for the radial variations of age, metallicity, and IMF as inferred from our fiducial set of spectral features (see Appendix B). Notice that the Na I 8190 feature, together with the Wing-Ford band at $\lambda \sim 9900$ Å, has been actually used by van Dokkum & Conroy (2010) to infer an enhanced population of low-mass stars in the centre of elliptical galaxies. Unfortunately, in the spectra of our samples of ETGs, similar issues as for the Na features also affect the gravity-sensitive spectral indices, CaH_1 ($\lambda \sim 6380$ Å), CaH_2 ($\lambda \sim 6850$ Å) and aTiO ($\lambda \sim 5500$ Å), recently proposed by Spiniello et al. (2014a). In particular, both CaH lines are affected by telluric absorption, CaH_1 is also affected by emission, whereas the aTiO passband encompasses a strong sky emission line ($\lambda \sim 5576$ Å). We note that the spectral index, bTiO, of Spiniello et al. (2014a) is very similar to the Serven et al. (2005) Mg 4780 index, that we already include in the χ^2 minimization procedure. In Appendix B, we show that, in spite of these problems, the gradients of CaH_2 and aTiO can be safely estimated (the latter with large error bars), while for CaH_1 the radial gradient is more uncertain (being more dependent on the way we perform sky subtraction). Nevertheless, we can obtain useful constraints on the radial variation of this index. Therefore, we treat CaH_1, CaH_2 and aTiO in the same way as Na features, i.e. we do not include them in the χ^2 minimization procedure, but we compare instead the observed gradients with model predictions for our fiducial set of spectral features, breaking the degeneracy between IMF and the other stellar population parameters (e.g. elemental abundances).

3.3.2 Age determination

The age determination of a stellar population is often performed by means of the hydrogen Balmer lines, whose line strengths might replace the first term on the right-hand side of equation (1) in the χ^2 minimization procedure. In practise, we do not use this approach here, as (i) Hβ appears significantly contaminated by nebular emission for NGC 4552, with the emission correction being rather uncertain for this galaxy (Sarzi et al. 2006) and (ii) higher order Balmer lines (i.e. Hγ and Hδ), which are virtually unaffected by nebular emission, do not fall within the observed spectral range.

We constrain instead the age by direct fitting of each spectrum in the wavelength region $\lambda \sim 4600$–5600 Å, where prominent age and metallicity features are found, using a single SSP multiplied by a tenth-degree polynomial. We perform the fit for each of the 10 bimodal IMFs[2] provided by MIUSCAT models (Section 3.2). For a given IMF, the best-fitting parameters are the age and metallicity of the SSP, as well as the polynomial coefficients. Notice that the multiplicative polynomial accounts for deviations between the continua of data and models (e.g. flux calibration uncertainties in the data). For each IMF, we perform 1000 iterations of the fitting procedure, shifting randomly the flux values in the spectra according to their uncertainties. This procedure provides an age estimate [i.e. Age(Γ_b) in equation 1], along with its uncertainty,[3] $\sigma'_{\rm Age}(\Gamma_b)$, as a function of Γ_b. Notice that $\sigma_{\rm Age}$ in equation (1) is obtained by dividing $\sigma'_{\rm Age}$ by the root square of the number of spectral indices fitted, in order to give a similar weight to the first term on the right-hand side of equation (1) with respect to the second term (i.e. the index summation), that contains most of the information on the IMF. Although the age cannot be derived directly from the line strengths (i.e. Balmer lines, see above), the IMF inference is very robust against a variety of age determination methods, with different methods providing consistent Γ_b gradients (see Section 5). For NGC 4387, where the emission correction to Hβ is negligible (<0.03 Å), we verified that replacing the Age term in the χ^2 definition (equation 1) with an additional term in the EWs corresponding to the Hβ line, does not change the inferred values of Γ_b (also providing very consistent age estimates, within $\sim$1 Gyr,[4] to those derived from spectral fitting). Hence, our procedure is robust, and general enough, to constrain the age for all available spectra.

3.3.3 Chemical abundances and temperature effects

Chemical abundances can partly mimic the effect of a varying IMF. Moreover, we want to rely on empirical (rather than theoretical), solar-scale, stellar population (MILES) models to analyse the spectra. We take the abundance issue into account in two ways.

First, using the semi-empirical correction procedure described in LB13, we correct the observed line strengths to solar scale. The corrections to line strengths are the terms $C_{\alpha,i}\cdot$[α/Fe] in equation (1), where $C_{\alpha,i}$ are semi-empirical correction coefficients, given by the slopes of the correlations of line strengths with [α/Fe], at fixed velocity dispersion – from stacked spectra of ETGs in the Sloan Digital Sky Survey (SDSS; see LB13 for details). For each spectrum, we estimate [α/Fe] (and plug it into $C_{\alpha,i}\cdot$[α/Fe]) by a solar-scale proxy, $[Z_{\rm Mg}/Z_{\rm Fe}]$, defined as the difference of the metallicities estimated with either Mg or Fe lines, for a fixed Kroupa IMF, with MILES models. Notice that the [α/Fe] correction procedure assumes that the $C_{\alpha,i}$'s, derived in galaxy central regions (SDSS), are the same at different galactocentric distances. Although this assumption is not necessarily true, the terms $C_{\alpha,i}\cdot$[α/Fe] vanish outwards in our sample of ETGs (as [α/Fe]$\sim$0 at the largest radii probed). Thus, the computation of $C_{\alpha,i}$ does not affect significantly our conclusions. The correction for non-solar [α/Fe] abundance ratios is negligible for TiO features, while it tends to increase the EWs of Mg 4780 and Ca_2, especially in the centre of the massive galaxies, where [α/Fe] is high.

In addition, to allow for residual abundance variations, we also include the effect of varying [Ti/Fe] abundance, as an extra-fitting parameter, in equation (1) (see LB13 for details). The reason for including [Ti/Fe], rather than any other single element, in the analysis is that according to different theoretical stellar population models (Conroy & van Dokkum 2012; Johansson, Thomas & Maraston 2012), titanium is the main element whose individual abundance ratio affects the strength of TiO features, and, in fact, an increase of [Ti/Fe] with (central) velocity dispersion has been detected in ETGs (Johansson et al. 2012; LB13). Notice that TiO features might also be affected by [O/Fe] abundance (Conroy, Graves & van Dokkum 2014). Since oxygen closely follows magnesium, with deviations smaller than 0.1 dex, in both our Galaxy (independent of metallicity as shown by Bensby, Feltzing & Lundström 2004) and ETGs (Johansson et al. 2012), the effect of [O/Fe] is already accounted for by our solar-scale proxy correction (see above). Moreover, at least

[2] With slopes $\Gamma_b = \{0.3, 0.8, 1.0, 1.3, 1.5, 1.8, 2.0, 2.5, 2.8, 3.0\}$.

[3] Computed as the standard deviation of age estimates from the 1000 iterations.

[4] The same test was also performed on the additional high-mass galaxy, NGC 5557, for which results are only presented in Appendix A. The emission correction for this galaxy is negligible, and we find very consistent Γ_b's (within the errors, see Appendix) when constraining the age by either Hβ or spectral fitting.

some stellar population models (Johansson et al. 2012) do not predict any dependence of either TiO_1 or TiO_2 on [O/Fe]. Notice that the [Ti/Fe] abundance term in equation (1) does only affect TiO_1 and TiO_2, while it is negligible for Ca_2 and Mg 4780. For what concerns Ca_2, this feature might also be affected by Ca abundance variations. In contrast to Ti, no *residual* variation (i.e. not accounted for by our solar-scale correction) with (central) velocity dispersion has been detected with Ca. Therefore, we have not included Ca abundance in the analysis. The Mg 4780 index could be affected by radial gradients of several chemical species (e.g. C and Si), that are difficult to analyse even with the latest state-of-art stellar population models. For simplicity, we do not consider any of these effects here.

Finally, we note that gravity-sensitive features are also sensitive to the effective temperature of red giant branch (RGB) stars, $T_{\rm eff}$. Decreasing $T_{\rm eff}$, at optical wavelengths, mimics the effect of steepening the IMF, but this degeneracy breaks down completely in the red part (>7500 K) of the spectrum (Spiniello et al. 2014a). The fact that both optical and NIR features (e.g. Na I 8190) suggest an IMF radial gradient in our massive galaxies (see Appendix B) excludes $T_{\rm eff}$ as the main source for the radial variation of TiO features. Also, one should note that two of the main sources of possible variations of the $T_{\rm eff}$ of the RGB, i.e. Mg abundance and total metallicity (VandenBerg et al. 2012) (besides Si abundance), are already accounted for in the analysis by means of the solar-scale correction procedure (that virtually removes all effects tightly related to Mg abundance) and because we adopt stellar population models with varying total metallicity.

4 RESULTS

We start discussing below, in a qualitative manner, the radial behaviour of the IMF-sensitive TiO_2 feature (Section 4.1). In Section 4.2, we perform a quantitative comparison of best-fitting and observed line strengths, for all selected IMF-sensitive features, following the approach described in Section 3.2. The main results of this work are presented in Section 4.3, where we contrast the radial trends of IMF slope for the low-mass galaxy, NGC 4387, and our best high-mass candidate, NGC 4552. Results for our additional high-mass galaxy, NGC 5557, are presented separately in Appendix A, as this galaxy has been analysed with a different methodology than NGC 4387 and NGC 4552. Appendix B also shows that the NIR Na8190 doublet, as well as other optical features, provide (independent) radial constraints to the IMF, that are fully consistent with those from our fiducial set of spectral features.

4.1 Line-strength gradients: qualitative analysis

In Fig. 2 the spectral region around the IMF-sensitive TiO_2 spectral feature (Trager et al. 1998) is shown, for two radial bins corresponding to the centre (top) and one half of the effective radius (0.5 R_e, bottom) for NGC 4387 (left) and NGC 4552 (right), respectively. The TiO_2 index measures the absorption strength of a TiO molecular band, prominent in the atmospheres of low-mass cool stars (Mould 1976), and therefore, when detected in the integrated light of a stellar population, provides a sensitive tracer of the ratio of dwarf-to-giant stars. This ratio is a surrogate of IMF slope: the higher the ratio, the steeper the IMF.

The grey shaded regions in Fig. 2 show the allowed range in the TiO_2 feature for a wide range of age (7–14 Gyr), metallicity (−0.4 to +0.2 dex) and titanium abundance (from −0.5 to +0.2 dex), encompassing those measured from our data, but keeping the IMF fixed at the Milky Way 'standard' distribution. We find that:

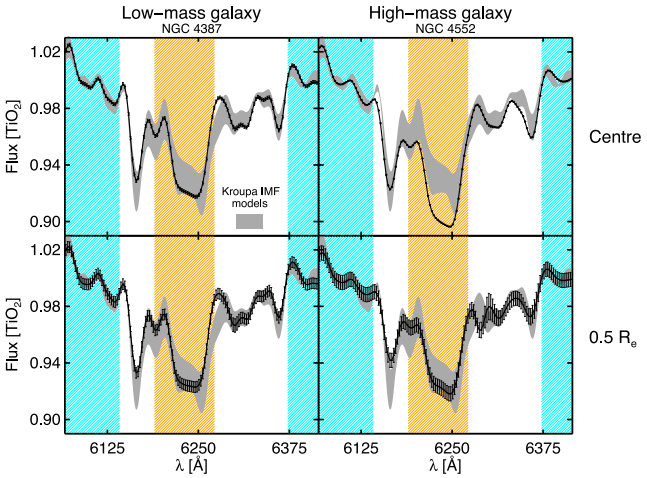

Figure 2. Spectral region surrounding the TiO_2 absorption band. The figure compares the spectra (the black curves with 1σ error bars) for the low-mass (left) and the high-mass (right) galaxies, in their centre (top) and at half of the effective radius (bottom). The grey region shows how the TiO_2 feature changes for SSP models with fixed, standard (Milky Way-like) IMF over a wide range of ages and chemical compositions. Note that any linear superposition of SSPs will also fall within the grey regions. Observed and model spectra are normalized to the blue flanking regions of the (orange-hatched) TiO_2 band, where the IMF information is encoded. In the low-mass galaxy, the TiO_2 can be well fitted with a universal IMF (grey region) at all radii. In contrast, the massive galaxy shows a significant gradient of TiO_2: a stronger absorption is detected in the centre, revealing an enhanced dwarf-to-giant ratio. At $R \sim 0.5\ R_e$, TiO_2 absorption is instead consistent with the range expected for a standard IMF.

(i) the TiO_2 spectral region of the low-mass galaxy is well reproduced by Kroupa-like IMF models at all radii; (ii) on the contrary, for our reference high-mass galaxy, a significant TiO_2 mismatch towards a bottom-heavy IMF is detected only in the central region. This TiO_2 gradient can only be explained by a change of IMF slope with radius (see Section 6).

4.2 Best fits to IMF-sensitive spectral indices

Fig. 3 illustrates the spectral analysis for our reference low- and high-mass galaxies, NGC 4387 (empty symbols) and NGC 4552 (solid symbols), respectively. Symbol colours vary from red, in the innermost, to blue, in the outermost radial bins. The triangles mark the measured EWs, while circles plot the quantities $[\mathrm{EW}_i - C_{\alpha,i} \cdot [\alpha/\mathrm{Fe}] - \Delta_{\mathrm{Ti,i}} \cdot \delta\mathrm{Ti}]$ in equation (1), i.e. the observed EWs corrected for [α/Fe], and with the TiO-based residual term removed. As mentioned above, the correction in [α/Fe] affects only Mg 4780 and Ca_2, and is negligible for TiO features (∼0.005 mag for the bin with the largest [α/Fe] correction). $\Delta_{\mathrm{Ti,i}}$ is different from zero only for TiO-based indices, and in particular for TiO_1 (when compared to its radial gradient; see the large differences among triangles and circles in panel b).

For NGC 4552, the best-fitting δTi shows an overall gradient of about −0.7 dex. Interestingly, this is similar to the total metallicity gradient of this galaxy. Note that despite of the large δTi radial variation, the gradient of TiO_2, after the residual abundance term is subtracted off, is still very significant (filled circles in panel c), and can only be explained by a radial gradient of IMF slope. In fact, to mimic the radial variation of TiO_2 with a fixed IMF, we would require a large radial gradient, more than +2 dex in δTi.

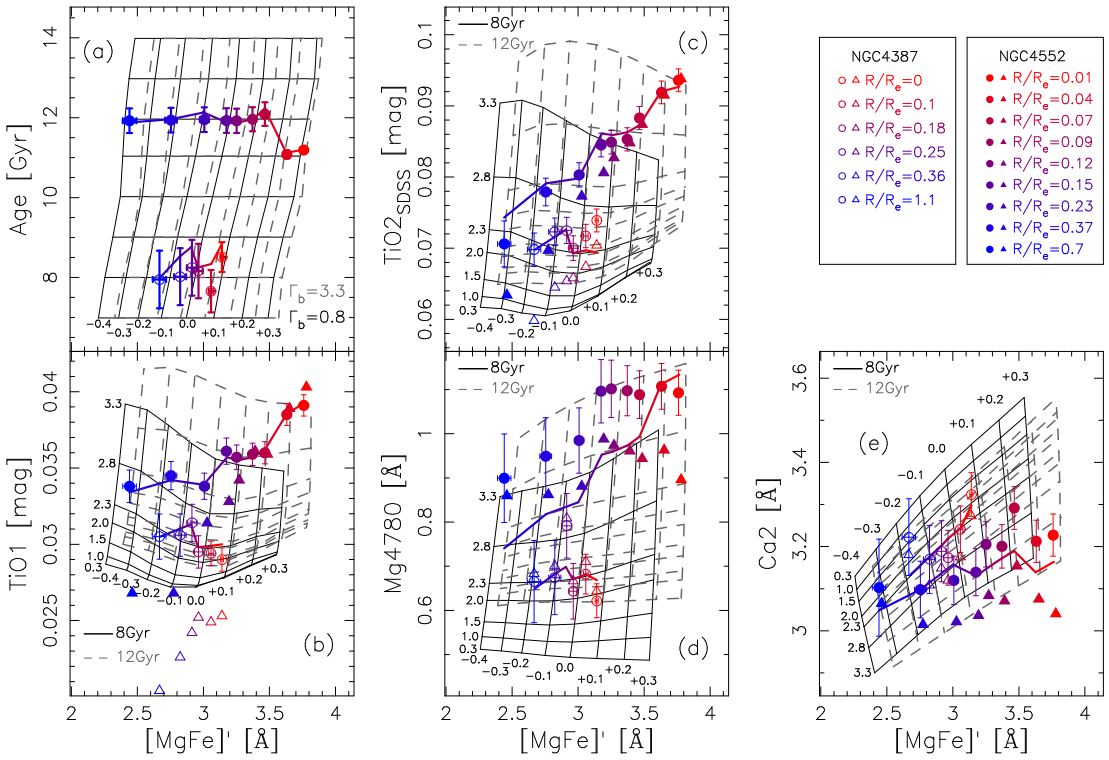

Figure 3. Fitting results for our low- (NGC 4387; open symbols) and high-mass (NGC 4552; filled symbols) galaxies. Panel (a): coloured symbols, with error bars, are age estimates from spectral fitting. Notice that the age estimates depend on the assumed IMF (see the text). Hence, for each galaxy, and each radial bin, the plot shows the age estimate for the corresponding, best-fitting IMF. The grids show the effect of varying metallicity on the [MgFe]′ index, for SSPs with different ages, and two extreme IMFs (grey-dashed and solid-black grids, as labelled). Panels (b)–(e): IMF-sensitive line strengths versus the total metallicity indicator [MgFe]′. The triangles show the raw line strengths, whereas circles (with error bars) show the line strengths corrected for [α/Fe], and with the best-fitting residual TiO-based abundance term (δTi in equation 1) subtracted off. The solid-coloured curves show the best-fitting solutions, with colour varying from red, in the galaxy centre, through blue, at larger galactocentric distances (see legend in the upper-right corner of the plot). The solid and dashed grids plot line strengths for SSP models with varying Γ_b and [Z/H], for two ages of 8 (representative of NGC 4387; see panel a) and 12 Gyr (oldest representative age for NGC 4552), respectively.

Such a strong gradient (at fixed IMF) would be inconsistent with the observed radial gradient of TiO_1 (see details in Section 6).

For Ca_2, our best-fitting solutions (Fig. 3) are fully consistent (1σ) with the data in each radial bin. Note that this index decreases with metallicity, and thus, because elliptical galaxies have negative metallicity gradients (see panel a of Fig. 3), one would expect a negative radial gradient of Ca_2. Apart from the outermost radial bin, where the error bar reflects a large uncertainty in sky subtraction, such a negative gradient is clearly observed for the low-mass galaxy. On the contrary, a flatter trend is found in NGC 4552, despite of its stronger metallicity gradient. Considering that Ca_2 decreases with Γ_b (Vazdekis et al. 2003), the mild Ca_2 gradient for the high-mass galaxy is fully consistent with the result that the slope of its IMF tends to decrease outwards. The case of Mg 4780 is less clear, as this index still shows a radial gradient in NGC 4552, possibly consistent with a less bottom-heavy IMF outwards. The gradient is mild, and only marginally consistent with the other indices, as one can see by comparing the filled circles and the best-fitting solution for NGC 4552 (upper curve) in panel (d) of Fig. 3. Based on stellar population models with varying abundance ratio (CvD12), we expect that this index anticorrelates with several chemical abundances, like [C/Fe] and [Si/Fe]. Hence, negative gradients, like those observed for [Z/H] and δTi, might be pushing this index towards higher values at large galactocentric distances. Since the effect is mild, and we still observe a gradient in Mg 4780, for the purpose of this work, we do not attempt any further analysis.

4.3 IMF radial gradients

The main result of this paper is shown in Fig. 4, where the radial trends of bimodal IMF slope, Γ_b, are presented for both NGC 4552 and NGC 4387, respectively.

For the massive galaxy NGC 4552, the IMF slope decreases, by $\Delta\Gamma_b = -1.5$, from the centre to 0.7 R_e. In the innermost radial bins, the inferred IMF slope ($\Gamma_b = 3.05 \pm 0.2$), implies a bottom-heavy distribution, consistent with previous work. In contrast, for the outermost bin, the best fit ($\Gamma_b = 1.9 \pm 0.4$) is higher, but still consistent at the 1.5σ level, with the value corresponding to a Kroupa-like distribution ($\Gamma_b \sim 1.35$). As shown in Appendix A, the additional massive galaxy (NGC 5557) also exhibits a decrement of Γ_b between the central part and the outer region, with $\Delta\Gamma_b = -1.5$ (-0.8), from the centre to 1(0.7) R_e. In contrast, the low-mass ETG, NGC 4387, shows almost no radial dependence of IMF within the uncertainties, with $\Delta\Gamma_b = -0.3$. In Appendix C, we also show that the correlation of uncertainties between the best-fitting parameters (mainly, age, δTi, and IMF) cannot explain, by itself, the radial IMF gradient detected in NGC 4552, i.e. the radial trend in Fig. 4 is not just the result of marginalizing the uncertainties along a given direction of the parameter space. We also notice that the inferred IMF slope for NGC 4387 is higher than that expected for its velocity dispersion (see LB13). However, while absolute values of Γ_b are significantly dependent on the set of adopted spectral features in the analysis (Spiniello et al. 2014a), it is expected that IMF-slope

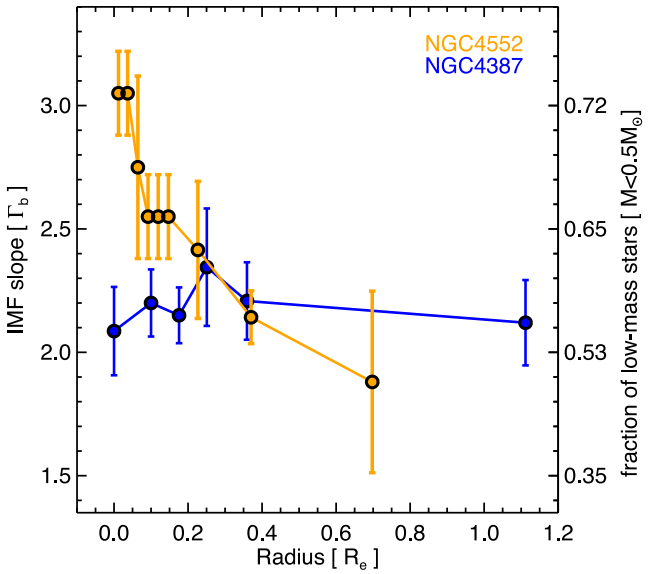

Figure 4. Radial IMF-slope profiles for the low- and high-mass galaxies, NGC 4387 and NGC 4552, respectively. The IMF slope, Γ_b, is inferred via a detailed analysis of gravity-sensitive features in the galaxy spectra, at different galactocentric distances. The fraction of low-mass stars ($M < 0.5$ M$_\odot$) with respect to the total stellar mass is shown in the vertical axis on the right. The massive ETG (yellow) shows a significant IMF-slope variation with radius. The less-massive system, NGC 4387, shows a rather flat IMF radial profile. Our measurements reveal that the enhanced population of dwarf stars (i.e. a higher Γ_b) in massive galaxies is confined to the central regions.

variations (i.e. the radial gradients) are constrained in a much more robust way. In addition, one may notice that (i) for a bimodal IMF, the difference of IMF normalization (i.e. the stellar mass-to-light ratio) between $\Gamma_b = 1.35$ (i.e. a Kroupa-like distribution) and $\Gamma_b \sim 2$ (as we measure for NGC 4387) is only 0.1 dex (SDSS *r*-band; Ferreras et al. 2013) and (ii) for a Kroupa-like slope ($\Gamma_b = 1.35$), IMF-sensitive features are much less sensitive to a given variation of Γ_b, than for a bottom-heavy IMF (e.g. $\Gamma_b \sim 3$). Hence, our results for the low-mass galaxy do not contradict independent constraints from dynamical studies (e.g. the results from the ATLAS3D survey), and the mild difference between $\Gamma_b \sim 2$ and $\Gamma_b \sim 1.35$ (Kroupa-like) is likely not relevant for this work. In terms of the dwarf-to-giant stellar ratio in the IMF (see LB13), up to ∼75 per cent of the stellar mass in the centre of the massive galaxy NGC 4552 is accounted for by stars below $M < 0.5$ M$_\odot$, whereas for the outermost radial bin, this ratio decreases down to ∼50 per cent. For the low-mass galaxy, NGC 4387, stars with $M < 0.5$ M$_\odot$ account for a roughly constant 56 per cent of the total stellar mass at all radii. The results of our analysis for NGC 4552 and NGC 4387 are summarized in Table 1, where we list the best-fitting age, [*Z*/H], and Γ_b for all radial distance bins, along with the typical S/N of each spectrum. The table also lists the [α/Fe] as inferred from the [Z_{Mg}/Z_{Fe}] proxy (see Section 3.3.3).

5 ROBUSTNESS OF INFERRED IMF GRADIENTS

To prove the robustness of our results, we have performed a battery of tests, varying the procedure to infer the IMF slope. These tests are described below.

Age estimate: This is one of the main uncertainties in the IMF determination, as most IMF-sensitive spectral indices are sensitive to age. In addition to including the Ca2 index in the analysis (which is sensitive to IMF, but not to age), we have addressed the age estimate issue as follows. (i) We have tested the effect of more complex star formation histories (than a single SSP), estimating the age from spectral fitting with two-SSP models. (ii) As a further *extreme* test, we have also calculated the radial IMF profiles by neglecting completely the age constraint from spectral fitting, i.e. repeating the fits by removing the first term in the right-hand side of equation (1). (iii) We have tested the impact of our assumption that residual δTi correction affect only spectral indices, and not the age determination itself. To this aim, we have implemented an iterative approach, where spectral and index fitting are repeated, after dividing each input spectrum with the ratio of [Ti/Fe]-enhanced to solar-scale SSP theoretical models (CvD12), the ratio being scaled to match the [Ti/Fe] residual abundance from the first minimization of equation (1). In practise, the output best-fitting parameters from the first iteration are very similar (within a few per cent) to those from the zero-order step, requiring no further iterations.

Table 1. Best-fitting parameters for the massive galaxy NGC 4552, and the low-mass galaxy NGC 4387. Uncertainties are quoted at the 1σ level.

Galaxy	R (R_e)	S/N	Age (Gyr)	[*Z*/H] (dex)	[α/Fe] (dex)	Γ_b
NGC 4552	0.01	1450	11.2 ± 0.1	$+0.29 \pm 0.01$	0.41 ± 0.01	3.05 ± 0.2
	0.03	911	11.1 ± 0.1	$+0.21 \pm 0.01$	0.30 ± 0.01	3.05 ± 0.2
	0.06	413	12.3 ± 0.2	$+0.09 \pm 0.01$	0.30 ± 0.01	2.75 ± 0.2
	0.09	281	12.0 ± 0.2	$+0.04 \pm 0.01$	0.29 ± 0.02	2.55 ± 0.2
	0.11	166	11.9 ± 0.2	-0.02 ± 0.02	0.27 ± 0.02	2.55 ± 0.2
	0.14	122	11.9 ± 0.2	-0.06 ± 0.02	0.23 ± 0.02	2.55 ± 0.2
	0.22	94	11.9 ± 0.2	-0.14 ± 0.02	0.21 ± 0.02	2.4 ± 0.3
	0.37	95	12.0 ± 0.3	-0.25 ± 0.02	0.18 ± 0.03	2.1 ± 0.1
	0.69	98	12.0 ± 0.3	-0.40 ± 0.03	0.08 ± 0.04	1.9 ± 0.4
NGC 4387	0.00	529	8.7 ± 0.3	$+0.06 \pm 0.01$	0.11 ± 0.01	2.1 ± 0.2
	0.10	349	7.5 ± 0.6	$+0.05 \pm 0.02$	0.14 ± 0.01	2.2 ± 0.2
	0.17	187	8.0 ± 0.6	-0.02 ± 0.02	0.12 ± 0.02	2.1 ± 0.1
	0.25	143	8.1 ± 0.6	-0.05 ± 0.03	0.09 ± 0.02	2.3 ± 0.3
	0.35	110	7.9 ± 0.7	-0.09 ± 0.03	0.13 ± 0.02	2.2 ± 0.2
	1.11	93	7.8 ± 0.6	-0.16 ± 0.03	0.09 ± 0.03	2.1 ± 0.2

Temperature sffects on the SSP modelling: We have varied (iv) the temperature scale of low-mass ($M < 0.5$ M$_\odot$) dwarf stars in MILES models – which has a major impact on various IMF-sensitive indicators – according to a cooler prescription (Pols et al. 1995) than the MILES reference one (Vazdekis et al. 2012); (v) we have arbitrarily shifted the scale of RGB stars by ±50 K, as these changes affect significantly molecular bands (i.e. TiO features).

Flux calibration uncertainties: We have fitted the continuum of each observed spectrum, in the TiO spectral regions, with MILES SSPs multiplied by a low-order polynomial in each region (with degree $\delta(\lambda)/100$, where $\delta(\lambda)$ is the spectral range size, see CvD12). Fitting different models (e.g. varying slightly the IMF, age, metallicity of MILES SSPs, and/or the polynomial degree, and for different spectra) we estimated that the impact of flux calibration uncertainties may affect significantly TiO$_1$, and to less extent TiO$_2$. Even accounting for rotation, the net effect is to offset the observed line strengths (i.e. radial gradients are not affected at all). Thus, as a further test, (vi) we have repeated the analysis by shifting TiO$_1$ and TiO$_2$ line strengths by the maximum shifts allowed by our continuum fits, i.e. +0.009 and +0.005 mag, respectively. The outcome of this test is that TiO flux calibration offsets can introduce a large shift in the derived δTi, up to ∼0.6 dex, while IMF gradients remain unchanged. Hence, the absolute value of the δTi does not reflect the actual [Ti/Fe] overabundance of the stellar population.

The results of the above tests (i)–(vi) are shown, – for our reference massive galaxy, NGC 4552 – in Fig. 5. The figure plots IMF radial trends for all tests, proving that indeed our results are very robust. In particular, none of our experiments – changing the assumptions of fitting methodology, stellar population modelling, and exploring the impact of flux calibration issues in the data – alters the existence of a significant radial IMF gradient for NGC 4552.

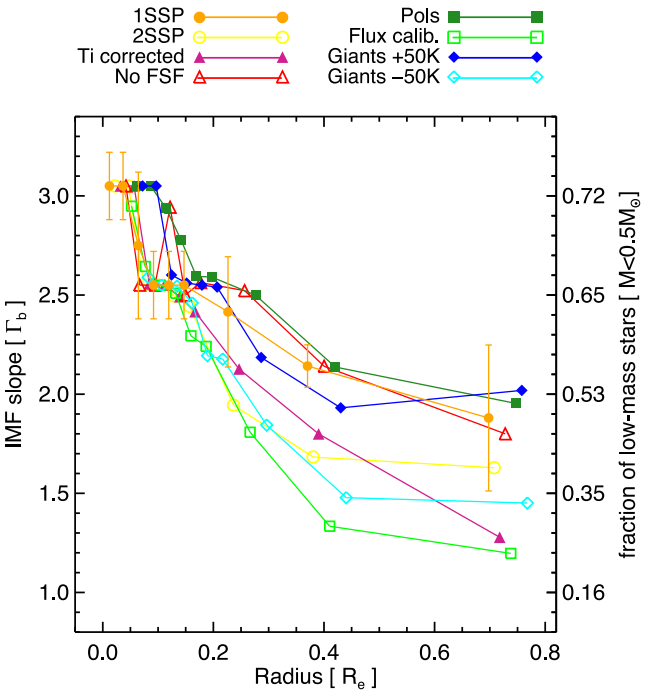

Figure 5. Different IMF radial profiles for NGC 4552, obtained by changing several assumptions in the modelling/fitting process. Profiles obtained with different assumptions are plotted with different colours and symbols, as labelled on the top of the figure. Remarkably, all radial profiles show a gradient in the IMF slope, from a bottom-heavy IMF in the galaxy centre to a more 'standard' slope, closer to a Kroupa-like value of $\Gamma_b = 1.3$, at about one effective radius. Hence, our results are robust against all performed tests: age derived through one (*1SSP*) or two (*2SSP*) SSPs; considering the δTi impact on the age estimation (*Ti corrected*); inferring the age with no information from full spectral fitting (*No FSF*); using a cooler prescription for the dwarf stars temperature (Pols); testing the flux calibration (*Flux calib.*) and changing the temperature scale of giant stars by plus 50 K (*Giants +50 K*) and minus 50 K (*Giants −50 K*).

6 CAN WE FIT THE OBSERVATIONS WITH A CONSTANT IMF?

In the following, we elaborate the tests presented in Section 5, discussing why a radial variation of the IMF seems to be the only possible explanation to the radial trends of IMF-sensitive indices in our massive galaxies. To this effect, we discuss several scenarios that might mimic the effect of a varying IMF with galactocentric distance.

(i) *Varying the temperature scale of dwarf (<0.5* M$_\odot$*) stars*. As mentioned in test (iv) of Section 5, we have constructed SSP models with a significantly cooler prescription (Pols et al. 1995) for low-mass dwarves than MILES SSPs (Vazdekis et al. 2012), by ΔT∼ 200 K. This temperature variation turns out to affect mostly the TiO indices. For an IMF slope of $\Gamma_b = 3$, the TiO$_2$ decreases by ∼0.007 mag (when using the cooler temperature scale). For $\Gamma_b = 1.35$ (i.e. Kroupa-like IMF), the TiO$_2$ changes only by ∼−0.002 mag. Since the metallicity proxy, [MgFe]′, is almost insensitive to the dwarf temperature scale, the net effect is to shrink the model TiO$_2$–[MgFe]′ grid in panel (c) of Fig. 3, along the 'IMF axis' (y-axis). Hence, although a change in the temperature scale of low-mass dwarves affects the absolute values of the IMF slope in the galaxy centre, the IMF gradient cannot be removed, as shown in Fig. 5.

(ii) *Varying the temperature scale of giant stars*. We have constructed SSP models by shifting the temperature of RGB stars by $\delta(T_{\rm eff}) = -150$, -100, -50, 0, and +50 K, respectively (a shift of zero corresponding to our reference MILES models). For $\delta(T_{\rm eff}) = -150$ K, the model TiO$_2$ increases by ∼0.02 mag, i.e. a large variation, comparable to that between a bottom-heavy and standard IMFs. A similar result applies to Mg 4780 and TiO$_1$. Therefore, a radial gradient of $T_{\rm eff}$ might be able to explain, by itself, the TiO radial gradients. However, this possibility is ruled out by our NIR spectral indices, as well as other gravity-sensitive features (CaH$_1$ and CaH$_2$, see Appendix B). In particular, for $\delta(T_{\rm eff}) = -150$ K, the model Ca$_2$ index changes by only ∼0.03 Å, while the model Na I 8190 shows an opposite variation with respect to its observed radial gradient, *decreasing* by ∼0.2 Å. We notice that two of the main sources of opacity in a stellar population – total metallicity and [Mg/Fe], besides [Si/Fe] (VandenBerg et al. 2012) – are properly accounted for in our analysis, the former by the fact that we rely on models with varying total metallicity, and the latter by our [α/Fe] correction procedure. This leaves very small leeway for residual $T_{\rm eff}$ variations. Furthermore, as already mentioned, a positive radial gradient of $T_{\rm eff}$ cannot match simultaneously the observed radial trends of both TiO, Na, and Ca/CaH indices. Since a change of $T_{\rm eff}$ also affects the shape of the TiO–[MgFe]′ index–index grid (see Fig. 3), we have also tested the impact of a fixed $\delta(T_{\rm eff})$ (=+/− 50 K) on our results. Since the change in the shape of the TiO$_1$ versus [MgFe]′ and TiO$_2$ versus [MgFe]′ grids is very similar, no significant variation is found in the IMF trends (see Fig. 5).

(iii) *Radial [α/Fe] variation.* As found in LB13, the [α/Fe] correction of TiO indices is small (e.g. less than ∼0.005 mag for TiO$_2$).

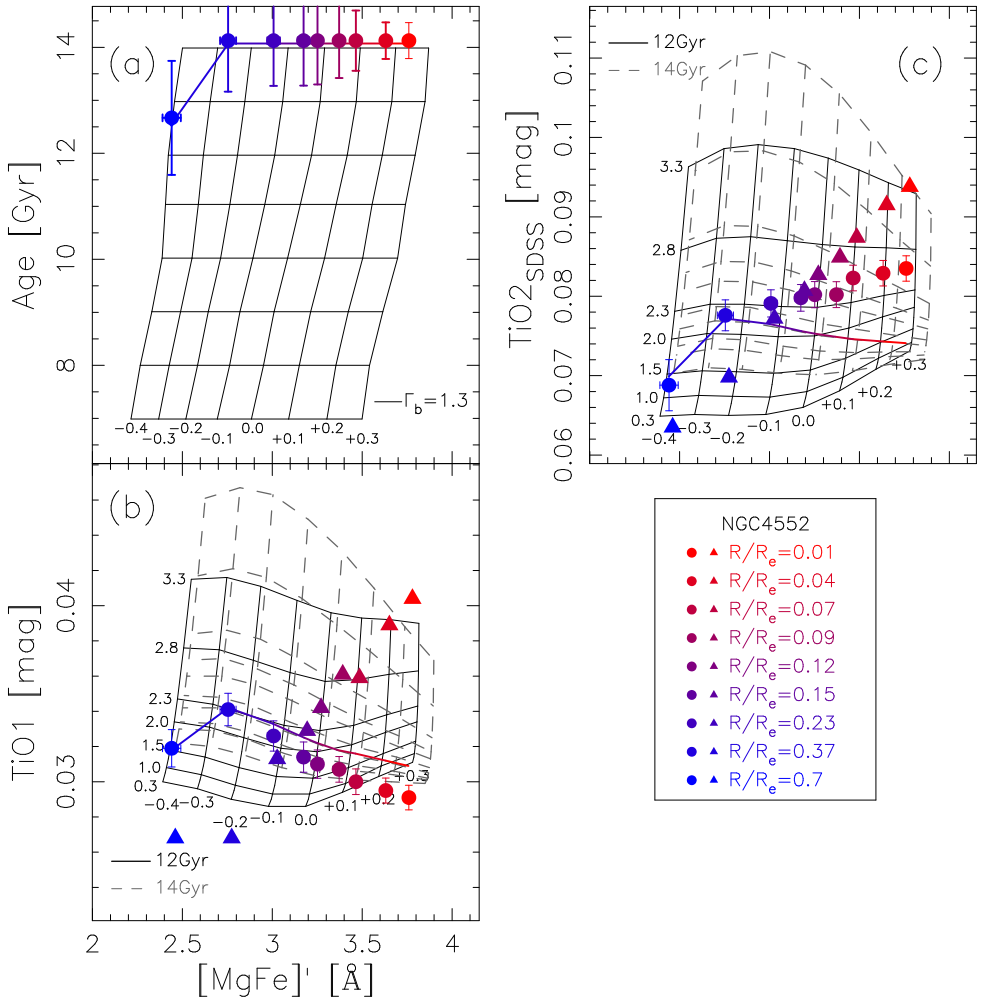

Figure 6. Fitting results for our reference high-mass galaxy, NGC 4552, obtained by leaving age, metallicity, and δTi as free parameters, but assuming a fixed, standard (Kroupa-like), IMF. Panel (a): coloured dots, with error bars, are age estimates from spectral fitting, for a Kroupa IMF. The grid shows the effect of varying metallicity on the [MgFe]′ index, for SSPs with a Kroupa-like IMF ($\Gamma_b = 1.35$) and different ages. Panels (b) and (c): the solid and dashed grids show line strengths for SSP models with varying Γ_b and [Z/H], for two representative ages of 12 (outermost radial bin; see panel a) and 14 Gyr (innermost bins), respectively. The filled circles, with error bars, are the [α/Fe]-corrected and δTi-shifted line strengths, while triangles plot raw line strengths (as measured on the spectra). Notice that triangles are the same as in panels (b) and (c) of Fig. 3. Since δTi is a free-fitting parameter, the δTi values are not the same when assuming a fixed, relative to a varying, IMF. Hence, coloured dots in panels (b) and (c) are not the same as those in Fig. 3. In all panels, solid-coloured curves show the best-fitting solutions, with colour varying from red, in the galaxy centre, through blue, at larger galactocentric distances. The same colour coding applies to dots and triangles (see the legend in the lower-right corner of the plot). For the two outermost bins, the best-fitting Kroupa-like models (coloured curves) match the [α/Fe]-corrected and δTi-shifted line strengths (filled circles). On the contrary, in the five innermost bins, the model TiO_2 deviates by more than 3σ from the observations, while significant deviations (at 2σ) are also seen for TiO_1.

Therefore, radial gradients of [Mg/Fe] (and that of other α elements that closely follow Mg, such as [O/Fe]) cannot explain the radial variation of TiO indices. Furthermore, the measured gradient in [α/Fe] in both massive galaxies would imply a Na I 8190 gradient opposite to the observed one (i.e. in this scenario, Na I 8190 should increase outwards).

(iv) *Radial [*Ti/Fe*] abundance variation.* A radial gradient of [Ti/Fe], as large as 2 dex, would be required to account for the observed gradient of the TiO_2 index. Because of the expected similar response of both TiO indices to Ti abundance, one cannot fit both TiO_1 and TiO_2 gradients with a radial variation of [Ti/Fe] alone. If we leave only age, metallicity, and [Ti/Fe] abundance as free parameters, for models with a fixed IMF, the best-fitting solution for the massive galaxy NGC 4552 deviates by more than 2σ (3σ) from the observed TiO_1 (TiO_2) values, as shown in Fig. 6. Thus, a radial variation of [Ti/Fe] cannot mimic the effect of a radially varying IMF.

(v) *Radial [*Na/Fe*] abundance variation.* In Appendix B1, we analyse the radial behaviour of the Na features at 5900 Å (NaD) and 8200 Å (Na I 8190), respectively. For a constant IMF, after subtracting off the expected variation due to the metallicity gradient of NGC 4552, one could explain the radial variation of Na I 8190 with a gradient of about 1 dex in [Na/Fe] abundance (with an uncertainty of $\pm$0.2 dex, depending on the data reduction procedure). Such a scenario would imply a change of about 3.3 Å in the NaD line strength. In contrast, a modest change is allowed by the observations (<1 Å, after removing the effect of metallicity; see bottom panel of Fig. B2 and Appendix B1). Hence, similarly to TiO indices, we cannot explain multiple indices (in this case, the NaD and Na I 8190 radial gradients) by

invoking a variation of [Na/Fe] alone, with the assumption of a fixed IMF.

Finally, we want to emphasize that the agreement in the radial behaviour of a wide set of spectral features (from different chemical species and covering a large wavelength range) as that considered in this paper (i.e. TiO_1, TiO_2, Ca_2, Mg 4780 plus aTiO, CaH_2, NaD, Na I 8190) breaks the degeneracy between IMF and elemental abundances and/or $T_{\rm eff}$ (see Appendix B and Section 5), proving the robustness of our result, i.e. the IMF radial variation in the two massive ETGs studied here.

7 DISCUSSION

We have found that the massive ETG NGC 4552 shows a radial variation of gravity-sensitive indices that can only be explained if an IMF radial gradient is invoked, from a bottom-heavy slope (i.e. an enhanced dwarf-to-giant ratio) in the centre, to a significantly flatter distribution, closer to the standard (Kroupa-like) IMF, at a galactocentric distance of about one effective radius. Evidence for a decrement in IMF slope are also found for the additional high-mass galaxy NGC 5557, whose IMF slope is fully consistent with a Kroupa-like IMF in the outermost radial bin. On the contrary, a low-mass ETG, NGC 4387, presents a flat radial trend of IMF slope.

Hence, although previous studies suggested a trend with galaxy mass on a global sense (Cenarro et al. 2003; van Dokkum & Conroy 2010; Ferreras et al. 2013; LB13), our findings imply that *it is in the cores of massive galaxies* where star formation processes are fundamentally different, leading to a bottom-heavy IMF. The $\Gamma_{\rm b}$ profiles of Fig. 4 imply that the correlation of IMF slope and galaxy mass found in previous studies (Cenarro et al. 2003; van Dokkum & Conroy 2010; Cappellari et al. 2012; Ferreras et al. 2013; LB13) likely arises because of an enhanced fraction of low-mass stars in the central regions ($R \lesssim 0.3$–$0.5\,R_{\rm e}$) of the most massive ETGs. The $\Gamma_{\rm b}$–mass relation (Ferreras et al. 2013; LB13) predicts $\Gamma_{\rm b} \sim 3$ for $\sigma \sim 300\,{\rm km\,s^{-1}}$, a value fully consistent with the innermost radial bins of NGC 4552. It is therefore the central region that drives the observed correlation between IMF slope and velocity dispersion among galaxies.

Our results suggest that the IMF in ETGs is driven by the local conditions of the ISM during the process of formation. At present, there is no complete theory of star formation that could address in a comprehensive way the connection between the initial stages of star formation and the properties of the IMF, especially the characteristic stellar mass and the location of the turnover in the power law at low masses. The fragmentation scales are driven by complex physics involving thermal properties of the gas; the contribution of dust to cooling; magnetic fields; turbulence; the effect of supersonic motions in the turbulent gas; and the transition from pre-stellar cores to stars, among others (Padoan & Nordlund 2002; Larson 2005; Bonnell, Clark & Bate 2008; Hopkins 2013). In addition, constraints based on observations of unresolved stellar populations can only provide an effective IMF integrated with respect to the past star formation history of the galaxy (i.e. the integrated galactic IMF, IGIMF; Kroupa & Weidner 2003). For instance, a naïve assumption of a bottom-heavy IMF in the cores of massive galaxies would lead to a significant paucity of metals, in conflict with the observed metal-rich populations in these regions. It is by assuming that the IMF is time dependent, and coupled to the star formation rate, that one can obtain results that are compatible with the observations (Vazdekis et al. 1997; Elmegreen & Scalo 2006; Weidner et al. 2013). Nevertheless, it is not clear at present how the most developed theoretical mechanisms describing variations in the IGIMF over galactic scales (Weidner & Kroupa 2005) can also explain local variations. Therefore, observational constraints such as the one presented in this paper provide essential information towards a complete theory of star formation.

Furthermore, the observed radial difference in the IMF of massive galaxies can be understood as the imprint from two different modes of galaxy formation (Oser et al. 2010): a quick and efficient one, building up the cores of massive ETGs at high redshift, during an early epoch (Eggen, Lynden-Bell & Sandage 1962) – leading to a system with high velocity dispersion and a bottom-heavy IMF – followed by a more gradual growth of the outermost regions (Navarro-González et al. 2013), perhaps either by the accretion of smaller structures (Naab, Johansson & Ostriker 2009), or via a quiet, prolonged, star formation rate, where the lower velocity dispersion of the ISM leads to a standard IMF. Studies of massive ETGs with uncorrelated radial gradients of the IMF distribution and [α/Fe] enhancement are crucial to determine the local parameter driving the IMF in these galaxies. This two-phase formation scenario is in sharp contrast with a naïve interpretation of the hierarchical buildup paradigm of galaxy formation, where high-mass systems form through the mere assembly of smaller units, and calls for further observational and theoretical advances.

8 CONCLUSIONS

We have analysed the spectra of two nearby ETGs: a massive galaxy, NGC 4552, and a low-mass counterpart, NGC 4387. Results for an additional high-mass galaxy, NGC 5557 (with lower quality data), are also discussed. Comparing observed line strengths to predictions of state-of-art stellar population models, we have found the following.

(i) Massive galaxies show a steep radial variation of the IMF slope, with an enhanced fraction of low-mass stars in the centre and a standard Kroupa-like distribution at the effective radius (Fig. 4).

(ii) The IMF gradient of the low-mass galaxy is rather flat, mildly steeper than that for a Kroupa-like IMF throughout (Fig. 4).

(iii) Our result naturally explains the IMF slope versus central velocity dispersion relation of ETGs, as a luminosity-weighted average of the underlying IMF radial gradient.

We therefore suggest that the IMF of nearby ETGs should be regarded as a 'local' property, with an excess of low-mass stars being produced by processes driving the formation of their cores – during the early phases of star formation.

Although simple, phenomenological models provide explanations to this scenario (Hopkins 2013; Weidner et al. 2013), detailed ab initio numerical simulations are required to understand this fundamental link between the growth of structures and the 'baryon' physics of galaxy formation.

ACKNOWLEDGEMENTS

We would like to thank the anonymous referee, for the many helpful comments, that helped us to significantly improve this manuscript. We would like to thank the GTC astronomers Antonio Cabrera, David García and Antonio García for their work during the observations. This work has benefited from interesting discussions with C. Weidner and M. Beasley. IM-N would like to specially thank Luis Peralta de Arriba for his comments during this work. This work has been supported by the Programa Nacional de Astronomía y Astrofísica of the former Spanish Ministry of Science and Innovation under grant AYA2010-21322-C03-02. Based on observations

made with the Gran Telescopio Canarias (GTC), installed in the Spanish Observatorio del Roque de los Muchachos of the Instituto de Astrofísica de Canarias, in the island of La Palma.

REFERENCES

Auger M. W., Treu T., Gavazzi R., Bolton A. S., Koopmans L. V. E., Marshall P. J., 2010, ApJ, 721, L163
Bastian N., Covey K. R., Meyer M. R., 2010, ARA&A, 48, 339
Bensby T., Feltzing S., Lundström I., 2004, A&A, 415, 155
Bonnell I. A., Clark P., Bate M. R., 2008, MNRAS, 389, 1556
Cappellari M., Emsellem E., 2004, PASP, 116, 138
Cappellari M. et al., 2011, MNRAS, 413, 813
Cappellari M. et al., 2012, Nature, 484, 485
Cardiel N., 1999, PhD thesis, Universidad Complutense de Madrid
Carter D., Visvanathan N., Pickles A. J., 1986, ApJ, 311, 637
Cenarro A. J., Cardiel N., Gorgas J., Peletier R. F., Vazdekis A., Prada F., 2001, MNRAS, 326, 959
Cenarro A. J., Gorgas J., Vazdekis A., Cardiel N., Peletier R. F., 2003, MNRAS, 339, L12
Cepa J. et al., 2000, in Iye M., Moorwood A. F., eds, SPIE Conf. Ser. Vol. 4008, Optical and IR Telescope Instrumentation and Detectors. SPIE, Bellingham, p. 623
Cohen J. G., 1979, ApJ, 228, 405
Conroy C., van Dokkum P., 2012, ApJ, 747, 69 (CvD12)
Conroy C., Graves G. J., van Dokkum P. G., 2014, ApJ, 780, 33
Delisle S., Hardy E., 1992, AJ, 103, 711
Dutton A. A., Macciò A. V., Mendel J. T., Simard L., 2013, MNRAS, 432, 2496
Eggen O. J., Lynden-Bell D., Sandage A. R., 1962, ApJ, 136, 748
Elmegreen B. G., Scalo J., 2006, ApJ, 636, 149
Emsellem E. et al., 2011, MNRAS, 414, 888
Falcón-Barroso J., Peletier R. F., Vazdekis A., Balcells M., 2003, ApJ, 588, L17
Ferreras I., La Barbera F., de la Rosa I. G., Vazdekis A., de Carvalho R. R., Falcón-Barroso J., Ricciardelli E., 2013, MNRAS, 429, L15
Hardy E., Couture J., 1988, ApJ, 325, L29
Hopkins P. F., 2013, MNRAS, 433, 170
Jeong H., Yi S. K., Kyeong J., Sarzi M., Sung E.-C., Oh K., 2013, ApJS, 208, 7
Johansson J., Thomas D., Maraston C., 2012, MNRAS, 421, 1908
Kroupa P., 2001, MNRAS, 322, 231
Kroupa P., 2002, Science, 295, 82
Kroupa P., Weidner C., 2003, ApJ, 598, 1076
Kroupa P., Weidner C., Pflamm-Altenburg J., Thies I., Dabringhausen J., Marks M., Maschberger T., 2013, 115
La Barbera F., Ferreras I., Vazdekis A., de la Rosa I. G., de Carvalho R. R., Trevisan M., Falcón-Barroso J., Ricciardelli E., 2013, MNRAS, 433, 3017 (LB13)
Larson R. B., 2005, MNRAS, 359, 211
Mould J. R., 1976, A&A, 48, 443
Naab T., Johansson P. H., Ostriker J. P., 2009, ApJ, 699, L178
Navarro-González J., Ricciardelli E., Quilis V., Vazdekis A., 2013, MNRAS, 436, 3507
Oser L., Ostriker J. P., Naab T., Johansson P. H., Burkert A., 2010, ApJ, 725, 2312
Padoan P., Nordlund Å., 2002, ApJ, 576, 870
Pols O. R., Tout C. A., Eggleton P. P., Han Z., 1995, MNRAS, 274, 964
Saglia R. P., Maraston C., Thomas D., Bender R., Colless M., 2002, ApJ, 579, L13
Salpeter E. E., 1955, ApJ, 121, 161
Sarzi M. et al., 2006, MNRAS, 366, 1151
Schiavon R. P., Barbuy B., Bruzual A. G., 2000, ApJ, 532, 453
Serven J., Worthey G., Briley M. M., 2005, ApJ, 627, 754
Smith R. J., 2014, MNRAS, 443, L69
Smith R. J., Lucey J. R., 2013, MNRAS, 434, 1964
Spiniello C., Trager S. C., Koopmans L. V. E., Chen Y. P., 2012, ApJ, 753, L32
Spiniello C., Trager S., Koopmans L. V. E., Conroy C., 2014a, MNRAS, 438, 1483
Spiniello C., Trager S. C., Koopmans L. V. E., 2014b, preprint (arXiv:e-prints)
Thomas D., Maraston C., Bender R., 2003, MNRAS, 339, 897
Thomas J. et al., 2011, MNRAS, 415, 545
Tortora C., Pipino A., D'Ercole A., Napolitano N. R., Matteucci F., 2013, MNRAS, 435, 786
Trager S. C., Worthey G., Faber S. M., Burstein D., Gonzalez J. J., 1998, ApJS, 116, 1
Treu T., Auger M. W., Koopmans L. V. E., Gavazzi R., Marshall P. J., Bolton A. S., 2010, ApJ, 709, 1195
van Dokkum P. G., Conroy C., 2010, Nature, 468, 940
VandenBerg D. A., Bergbusch P. A., Dotter A., Ferguson J. W., Michaud G., Richer J., Proffitt C. R., 2012, ApJ, 755, 15
Vazdekis A., Casuso E., Peletier R. F., Beckman J. E., 1996, ApJS, 106, 307
Vazdekis A., Peletier R. F., Beckman J. E., Casuso E., 1997, ApJS, 111, 203
Vazdekis A., Cenarro A. J., Gorgas J., Cardiel N., Peletier R. F., 2003, MNRAS, 340, 1317
Vazdekis A., Sánchez-Blázquez P., Falcón-Barroso J., Cenarro A. J., Beasley M. A., Cardiel N., Gorgas J., Peletier R. F., 2010, MNRAS, 404, 1639
Vazdekis A., Ricciardelli E., Cenarro A. J., Rivero-González J. G., Díaz-García L. A., Falcón-Barroso J., 2012, MNRAS, 424, 157
Wegner G. A., Corsini E. M., Thomas J., Saglia R. P., Bender R., Pu S. B., 2012, AJ, 144, 78
Weidner C., Kroupa P., 2005, ApJ, 625, 754
Weidner C., Ferreras I., Vazdekis A., La Barbera F., 2013, MNRAS, 435, 2274

APPENDIX A: NGC 5557

As part of the same observing campaign with OSIRIS/10.4 m GTC, we also acquired deep spectroscopic data for the high-mass ETG NGC 5557. Similar to NGC 4552, this galaxy shows no kinematic peculiarity within its effective radius, with a velocity dispersion profile that declines smoothly from $\sim$300 km s^{-1} in the centre, to $\sim$200 km s^{-1} at about one effective radius. We reduced the data for NGC 5557 in the same way as for NGC 4552 and NGC 4387. In particular, we extracted spectra in different radial bins, after removing the effect of the rotational velocity and velocity dispersion at each position along the slit. The radial bins were defined adaptively, in order to reach a target S/N $\geq$ 100 Å^{-1} for each bin.

Unfortunately, due to the recession velocity of the galaxy, the spectrum of NGC 5557 is redshifted to an observed frame where both TiO_1 and (to a minor extent) TiO_2 are affected by telluric absorption. We evaluated this effect by applying (alternatively) two different telluric absorption models to the observed spectra of NGC 5557, at all radial positions (i.e. each row along the 2D spectrum of the galaxy). The two models were constructed in a similar way as detailed below for NGC 4552 and NGC 4387 (see Appendix B1, where the two models are referred to as *TELL*1 and *TELL*2, respectively). The TiO indices were re-measured on the corrected spectra, re-extracted in each radial aperture. For both telluric models, the correction was found to be relevant for the TiO_1 index, with a variation of up to $\sim$0.025 mag in the innermost radial bin (i.e. comparable to the entire dynamical range covered by this index in panel b of Fig. 3). On the contrary, the effect of telluric absorption on the TiO_2 was very small, amounting to less than $\sim$0.003 mag at all radial bins (i.e. about one tenth of the difference between $\Gamma_b = 0.3$ and 3.3).

For these reasons, we have analysed the spectra of NGC 5557 with a different approach, by excluding TiO_1 from the χ^2

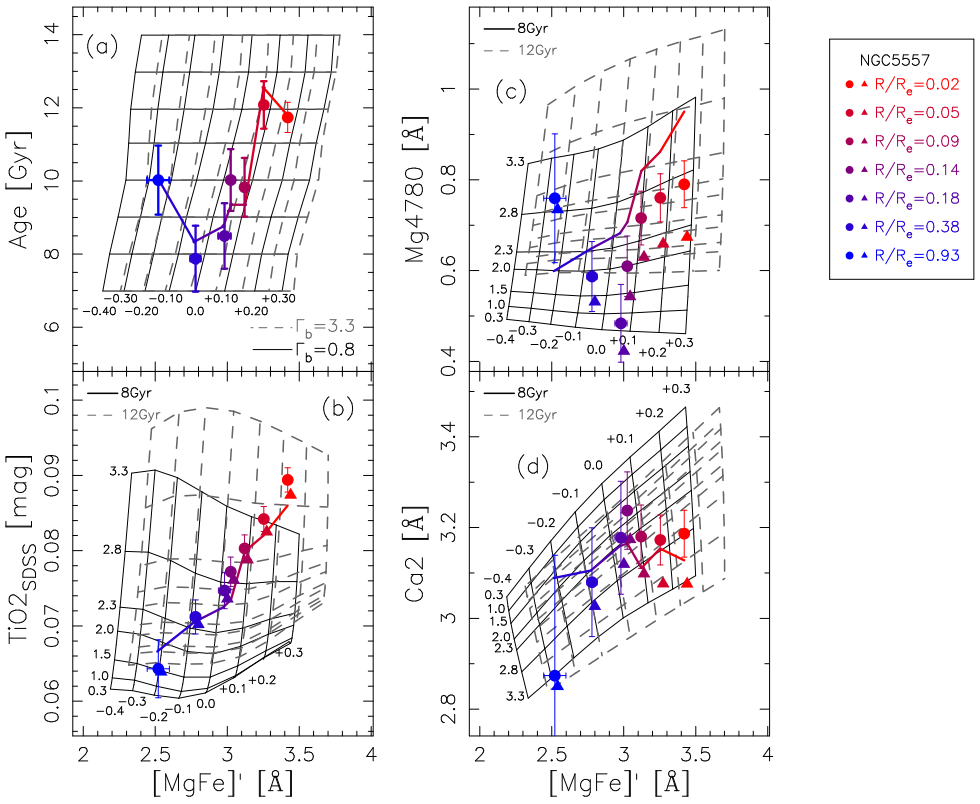

Figure A1. Fitting of line strengths for the massive ETG NGC 5557. This figure is similar to Fig. 3, but excluding the TiO_1 spectral feature, which is not reliable for this galaxy because of strong contamination from telluric absorption. Notice also that the solar-scale correction (difference between triangles and circles in panels b–d) does not include the effect of δTi residual abundance, as for NGC 4387 and NGC 4552 in Fig. 3.

minimization procedure (see equation 1). The TiO_2 index is also mildly contaminated by airglow, affecting only the central part of the feature, from 6224 to 6248 Å. We interpolated this spectral region both in models and observed data, for a consistent analysis. We point out that the effect of the interpolation is completely negligible, amounting to less than ∼0.002 mag on the TiO_2 line strengths, at all radial bins. Since there is a degeneracy between IMF slope and [Ti/Fe] abundance on a single TiO feature, for NGC 5557 we have minimized equation (1) by neglecting the effect of possible Ti abundance variations. This is motivated by the fact that, for NGC 4552, this residual abundance is found to have a minor effect on TiO_2 (see panel c of Fig. 3), both NGC 4552 and NGC 5557 showing a similar TiO_2 gradient (∼0.025 mag).

Figs A1 and A2 show the fitting of line strengths for NGC 5557 and the resulting gradient of IMF slope, respectively. The Γ_b radial profile for our reference massive galaxy, NGC 4552 (see Fig. 4), is overplotted in Fig. A2, in order to allow for a direct comparison of the two massive galaxies. As for NGC 4552, the Mg 4780 index of NGC 5557 deviates more than the other indices with respect to the best-fitting solution, although a radial gradient is detected for this feature (see panel c of Fig. A1). Overall, the Γ_b radial profile of NGC 5557 shows a similar behaviour as for NGC 4552, both profiles pointing to a decrease of IMF slope with galactocentric distance. However, one can notice that the Γ_b values for NGC 5557 are systematically lower than those for NGC 4552. This might be due to the fact that we have analysed these two galaxies with different sets of spectral features, or, alternatively, NGC 5557 might have a less bottom-heavy IMF than NGC 4552. For the purpose of this work, the relevant point is that the analysis of NGC 5557 also points to a radial IMF gradient, with the bottom-heavy population confined to the galaxy central regions. We notice that Fig. A2 suggests that the IMF radial gradient for NGC 5557 might be less significant than that for NGC 4552, mostly because of the relatively large error bars on Γ_b in the outermost radial bins. To address this issue, we have fitted the Γ_b versus R/R_e trend for NGC 5557 with a linear relation, adopting an ordinary least-squares fitting procedure with Γ_b as dependent variable. We have repeated the fitting 10 000 times, shifting each time the Γ_b values according to their uncertainties. We estimated the probability, P, that Γ_b does not decrease with radius, as the fraction of iterations giving best-fitting lines with non-negative slope values. The P turns out to be less than 1 per cent, also in the case where $\log R/R_e$, rather than R/R_e, is adopted as independent variable in the fitting. Also, as a further test, we computed a further binned spectrum for NGC 5557, at a radial position of R/R_e=0.7, i.e. the outest galactocentric distance explored for NGC 4552. For this bin, our fitting procedure gives $\Gamma_b = 1.78 \pm 0.2$ (see red triangle in Fig. A2). Including only galactocentric distance less than 0.7 R/R_e for NGC 5557, we still find a probability less than 1 that Γ_b profile does not decrease with radius in this system. Notice that, as discussed in Section 5 for the reference massive galaxy NGC 4552, other ingredients in the stellar population modelling (e.g. individual elemental abundances) might contribute to further flatten the radial Γ_b trend for NGC 5557. However, the existence of a genuine radial IMF gradient for this galaxy is also supported by the Na I 8190 feature, as shown in Appendix B1, as this feature breaks the degeneracy between IMF and other possible effects. Although our data suggest that the IMF gradient for NGC 5557 seems to be shallower than that for NGC 4552, together with analysis of

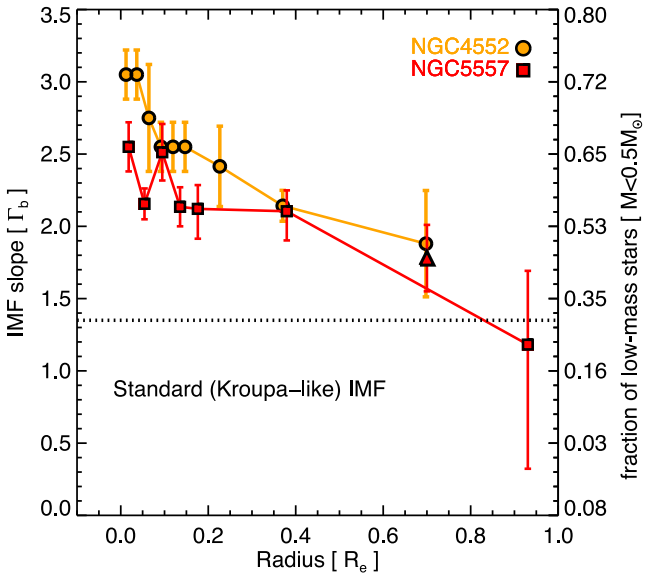

Figure A2. Radial IMF-slope gradient for the massive galaxy NGC 5557 (orange circles), compared to that for our reference massive ETG, NGC 4552 (red squares). The trend for NGC 4552 is the same as in Fig. 3. Error bars denote 1σ uncertainties. Notice that error bars are asymmetric, reflecting the fact that gravity-sensitive features are more sensitive to high, relative to low, values of Γ_b. Because of the different fitting methodology (see the text), the results for NGC 5557 are only presented in this appendix. Despite the relatively large error bars, the results for NGC 5557 also indicate a gradient of IMF slope, varying from bottom heavy in the centre to Kroupa-like outwards (see dotted horizontal line in the bottom panel), corroborating the result for our reference massive galaxy, NGC 4552. A radial bin at $R = 0.7R_e$ (red triangle) was calculated to compare directly both NGC 4552 and NGC 5557 IMF gradients at the same radial distance. Although this new bin is not independent from the original profile, it shows that the derived IMF gradient of NGC 5557 is not due to a larger error in the last radial bin.

NGC 4552 and NGC 4387, the results for NGC 5557 further support our conclusions that the enhanced fraction of low-mass stars in massive ellipticals is mostly located in their core regions.

APPENDIX B: RADIAL BEHAVIOUR OF ADDITIONAL GRAVITY-SENSITIVE FEATURES

B1 Radial trends of Na I 8190 and NaD

The NIR Na I doublet, at $\lambda \sim 8200$ Å, is a prominent feature in the atmospheres of low-mass dwarves, and it has been used, along with the Wing-Ford FeH band ($\lambda \sim 9900$ Å), to derive a significant excess of low-mass stars in the central regions of massive ETGs (van Dokkum & Conroy 2010). Unfortunately, for all the three galaxies observed with GTC-OSIRIS (Section 2), the Na I 8190 index is significantly contaminated by telluric absorption. No telluric standard is available for the same run as our observations, hampering the study of this line. However, since the *relative* absorption of flux is virtually the same at all radial positions for each galaxy, telluric absorption should not affect the amount of radial variation of the Na I 8190 EW, with only a constant shift in its absolute value. Since this statement is only exactly true in case of no radial rotational velocity, we have tested it directly by constructing two different telluric absorption models. The 'synthetic' model (hereafter *TELL*1) is obtained, for each galaxy, as the ratio between a two-SSP model and the observed spectrum in the innermost radial bin. The model

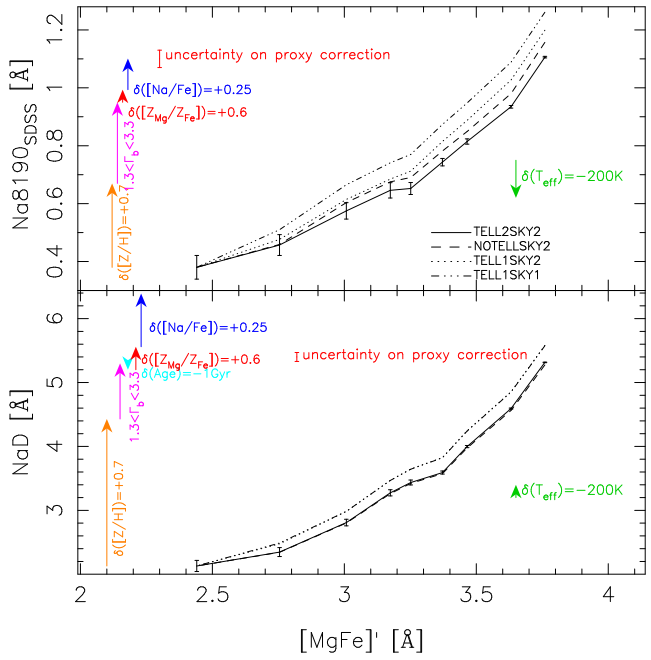

Figure B1. The Na I 8190 (top panel) and NaD (bottom panel) index radial profiles of NGC 4552 are plotted as a function of the total metallicity indicator [MgFe]′. The black curves with different line types (see the black legend in the upper panel) correspond to different methods to treat telluric absorption, i.e. methods *TELL*1 and *TELL*2 (see the text) and no telluric correction (*NOTELL*), as well as different sky subtraction procedures (methods *SKY*1 and *SKY*2, see the text). The black error bars are the maximum uncertainties (among different methods), quoted at the 1σ level. In both panels, arrows show the expected variation of the indices (for SSP models) because of the metallicity (orange), IMF (magenta), age (cyan), and $[Z_{Mg}/Z_{Fe}]$ (red) gradients for NGC 4552 (Section 4.2). Notice that the effect of varying age is not shown for Na I 8190, as it is completely negligible for this index. The effect of varying [Na/Fe] abundance and T_{eff} are also shown as blue and green arrows, respectively.

is obtained by fitting the spectrum, around the Na feature, with a linear combination of two SSPs, with age and metallicity being free-fitting parameters, and IMF fixed to the result of our fiducial χ^2 minimization procedure in the galaxy centre (where we obtain consistent results to our previous studies, targeting the central regions of ETGs with a variety of spectral features). The second absorption model (hereafter *TELL*2) relies on the spectrum of a telluric standard star, observed in a different observing run, but with the same instrumental setup as for NGC 4387 and NGC 4552. For each telluric model, we corrected the 2D galaxy spectra at each radial position, and re-extracted 1D spectra for all galactocentric distance bins, re-measuring the Na I 8190 EWs. The same kind of analysis was performed for the optical Na doublet, NaD, at $\lambda \sim 5900$ Å, as well as other IMF-sensitive features (see below). The NaD feature turns out to be affected by telluric absorption, and to major extent, by sky emission. To test also the latter effect, we re-measured both Na features by performing sky subtraction with two different methods, i.e. either interpolating the sky from either sides of the slit, far from the galaxy centre (hereafter method *SKY*1), or (method *SKY*2) performing a second iteration where the 2D spectrum of the galaxy (obtained from *SKY*1) is subtracted off from the original 2D frame, and the sky is re-estimated in a region closer to the galaxy centre.

Fig. B1 compares the radial gradients of Na I 8190 (upper panel) and NaD (lower panel), for our reference massive galaxy NGC 4552, among different methods used to treat telluric absorption and sky

emission (see the black curves with different line types, as labelled in the upper panel). Since the absolute value of the indices was found to be strongly dependent on the reduction procedure, we arbitrarily shifted all values, for a given method and each index, to match model predictions (from our best-fitting solution, see Section 4.2) in the outermost aperture. Notice that the amount of gradients in both indices is fairly consistent (considering the largest quoted error bars, i.e. for the outermost radial bin), among different methods (even when no telluric correction is applied at all), implying that the gradient of both Na features can be safely estimated. In both panels, different arrows plot the amount of expected variation of each index – when moving from the outermost to the innermost aperture – because of the gradients in different stellar population properties (metallicity, age, [α/Fe], and IMF). Summing up all different contributions (orange plus magenta plus red arrows), we predict a radial gradient of $\sim$0.6 and $\sim$3.4 Å for Na I 8190 and NaD, respectively. From the black curves, we see that the observed gradients are $\sim$0.7–0.85 Å for Na I 8190 ($\pm$0.1 Å, considering the error bar in the outermost bin, and that on proxy correction) and $\sim$3.3–3.5 Å ($\pm$0.12) for NaD. Hence, within the uncertainties, an IMF radial variation reconciles both Na features (once the effect of other parameters, in particular that of metallicity, is taken into account). The effect of varying the temperature of giant stars, $T_{\rm eff}$, in the stellar population models is also illustrated, with green arrows, in Fig. B1. Decreasing $T_{\rm eff}$ tends to decrease the model Na I 8190, i.e. it goes into an opposite direction to that of a more bottom-heavy IMF. On the other hand, NaD is insensitive to temperature variations, while TiO bands (panels b and c of Fig. 3) increase with decreasing $T_{\rm eff}$. Therefore, while the effect of a radially varying IMF is consistent among all features (including the Na ones), a radial variation in the temperature is clearly ruled out when combining optical and NIR features. A similar argument applies to [Na/Fe] abundance (see blue arrows in the figure, showing the effect of increasing [Na/Fe] by 0.25 dex, as estimated from CvD12 stellar population models). To mimic the effect of varying $\Gamma_{\rm b}$ from 1.3 to 3.3 (consistent with our estimated gradient for NGC 4552, see Fig. 5), a change of $\sim$0.25 dex in [Na/Fe] would be required for NaD. However, this is far too small (by a factor of 2) than that of a varying IMF on Na I 8190 (see magenta and blue arrows in the upper panel of Fig. B1). Hence, an [Na/Fe] gradient is not able to explain the observed gradients of both Na features (see, e.g. Spiniello, Trager & Koopmans 2014b), Finally, it is worth noting that alternative explanations for the 'unusual' strength of Na indices have also been proposed in the literature (Jeong et al. 2013).

As for NGC 4552, also for our reference low-mass galaxy, NGC 4387, we have found that the observed Na I 8190 gradients change very mildly, by $\lesssim$0.1 Å, among different reduction procedures, meaning that the Na I 8190 gradients can be robustly estimated from our data. Fig. B2 compares the radial gradients of Na I 8190 (whose EWs are estimated through methods *TELL2* and *SKY2*, see above) for the low- and high-mass galaxy. A constant shift is arbitrarily applied for each galaxy, to match the IMF slope derived from our fiducial set of spectral indices (see Section 3.3.1) in the outermost radial bins. The figure also plots the Na I 8190 gradient for the additional massive system, NGC 5557, observed as part of the same observational campaign as NGC 4387 and NGC 4552, but analysed apart in Appendix A. Remarkably, for the low-mass ETG, no radial gradient in Na I 8190 is detected, while a strong decrease is observed with galactocentric distance for the high-mass galaxies. As shown in Fig. B2, the metallicity gradient of NGC 4552 cannot explain, by itself, the Na I 8190 gradient (as also seen by comparing the size of the orange arrow, to the range of values for the black

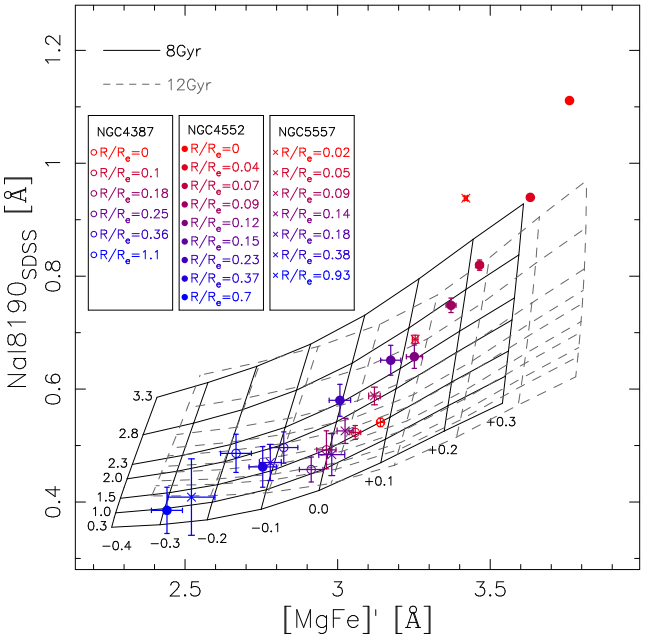

Figure B2. The Na I 8190$_{\rm SDSS}$ line strength is plotted as a function of the total metallicity indicator [MgFe]′, for NGC 4387 (empty circles), NGC 4552 (filled circles), and NGC 5557 (crosses; see Appendix A). Error bars are 1σ statistical uncertainties. The black and grey grids correspond to MILES SSP models with an age of 8 and 12 Gyr (i.e. the same as in Fig. 3), respectively. Notice that the Na I 8190 EWs are estimated with method *TELL2SKY2*, i.e. the same as for the black solid curve in Fig. B1. The strong gradients of Na I 8190$_{\rm SDSS}$ for the high-mass galaxies contrast with the flat behaviour of this feature for the low-mass system, NGC 4387. A constant offset has been applied to the line strengths of each galaxy, to account for the uncertainty on the absolute value of the indices, due to telluric absorption.

curves, in the upper panel of Fig. B1). Moreover, the Na I 8190 index is expected to decrease with [α/Fe] (according to CvD12 stellar population models), whereas NGC 4552, as well as NGC 5557, *both* have high [α/Fe] in the centre, and a very high Na I 8190 line strength. In conclusion, the radial gradients of Na features, for high-mass galaxies, also point to a significant radial variation of the stellar IMF, with an excess of low-mass stars confined to their central regions.

B2 Radial trends of CaH$_1$ and CaH$_2$

We discuss here the radial behaviour of the two IMF-sensitive indices, CaH$_1$ and CaH$_2$, recently proposed by Spiniello et al. (2014a). Both features (in particular CaH$_2$) are affected by telluric absorption in the spectra of our reference high-mass galaxy, NGC 4552. However, as done for Na features, we compare the radial gradients of both features among different reduction procedures, in order to gain further insights into the radial variation of stellar population properties for our reference massive galaxy. Fig. B3 is similar to Fig. B1, but plotting CaH$_2$ (top) and CaH$_1$ (bottom), rather than Na features, as a function of [MgFe]′ (both CaH features have been arbitrarily shifted in the figure). As seen by the size of the cyan arrows, both indices are insensitive to age, consistent with Spiniello et al. (2014a, Spiniello et al. 2014b). CaH$_2$ is also insensitive to total metallicity, while CaH$_1$ shows a mild trend to decrease with increasing [*Z*/H]. Notice that according to our empirical approach (LB13), both indices (in particular CaH$_2$) tend to *decrease* significantly with [$Z_{\rm Mg}/Z_{\rm Fe}$] (i.e. [α/Fe]; see red arrows), at fixed total

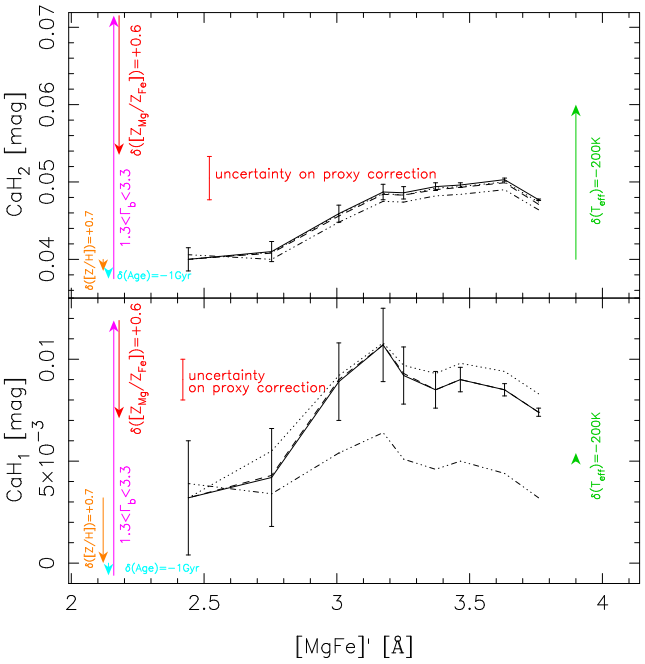

Figure B3. CaH_1 (bottom) and CaH_2 (top) radial gradients for NGC 4552, i.e. the same as Fig. B1 but for CaH, rather than Na, features. The telluric contamination of these indices does not allow us to trust the index absolute values. However, the radial gradient for CaH_2 is robust, while for CaH_1 we can exclude an increase of the index with radius (leftwards in the plot), as it would be the case for a constant IMF (see the text). Notice that CaH_2 is fully consistent with our results of a varying IMF for NGC 4552. In general, because of the different sensitivity of the two indices to a variation in $T_{\rm eff}$ (green arrows), one cannot explain the behaviour of both CaH features without a varying IMF with radius.

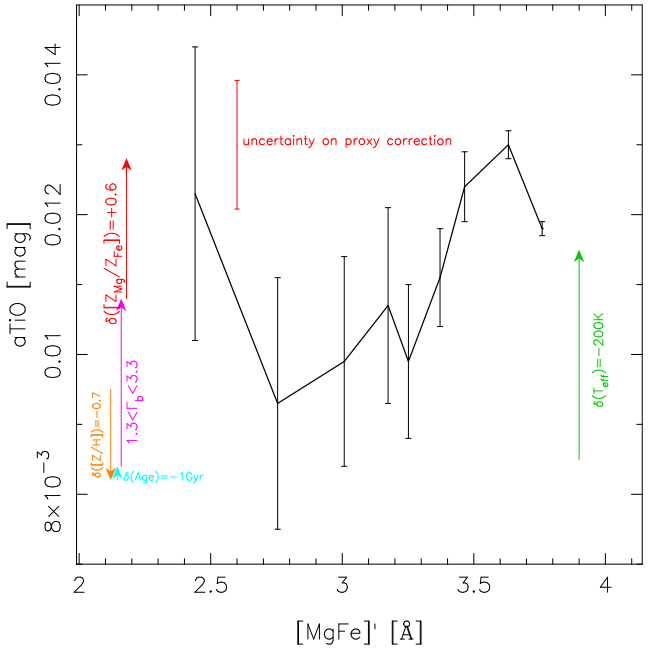

Figure B4. Radial profile of the interpolated aTiO index for NGC 4552 (see the text). Notice the large error bars, in the outer radial bins (left in the plot) preventing us to use this index to significantly constrain the IMF gradient. Notice that because the index is not affected by telluric absorption, while airglow contamination is avoided by our interpolation procedure, no difference exists among different reduction procedures and we did not apply any rigid shift to the line strengths (as, e.g. in Figs B1 and B3).

metallicity. As seen by summing up the orange, magenta, and red arrows in the upper panel of Fig. B3, the radial behaviour of CaH_2 is fully consistent with our results, i.e. a radial decrease of IMF slope in NGC 4552. For CaH_1, the situation is more uncertain, as this index turns out to be also significantly affected by airglow (see dot–dashed curve), and thus its radial gradient is either null or negative (i.e. decreasing outwards in the galaxy, leftwards in Fig. B3), depending on the reduction procedure. We notice that, for a fixed IMF slope, the CaH_1 gradient in NGC 4552 should be positive, as both metallicity and $[Z_{\rm Mg}/Z_{\rm Fe}]$ increase towards the galaxy centre, CaH_1 decreasing with both parameters. Hence, regardless of the reduction procedure, our results for CaH_1 also imply a radial decrease of IMF slope with radius in our reference massive galaxy. We notice that the radial gradient of CaH_2 might also be explained by decreasing $T_{\rm eff}$ in the models by ∼300 K. However, this would be inconsistent, at fixed IMF, with the radial trend of CaH_1, as the latter is insensitive to $T_{\rm eff}$. In conclusion, also CaH features imply an IMF gradient for NGC 4552, ruling out a radial variation of $T_{\rm eff}$.

B3 Radial trend of aTiO

Finally, we discuss the radial behaviour of the aTiO IMF-sensitive feature ($\lambda \sim 5500$ Å), also proposed by Spiniello et al. (2014a). Being present in the atmospheres of both dwarf and giant stars, the aTiO is a potentially good IMF indicator. In our data, a strong sky emission line ($\lambda \sim 5780$ Å) lays within the central bandpass of the index. To overcome this problem, we have linearly interpolated both data and models over the affected region. The radial profile of aTiO for NGC 4552 is shown in Fig. B4. In this case, since the feature is not affected by telluric absorption, we do not apply any shift to the line strengths. Also, since there is no difference among different reductions, only one black curve is shown in the figure. Unfortunately, because of the large error bars, the aTiO has little constraining power on the radial variation of the IMF for NGC 4552, and thus we have not included it in our χ^2 minimization procedure.

APPENDIX C: CORRELATED UNCERTAINTIES ON IMF AND OTHER PARAMETERS

In Fig. C1, we show the PDF contours of our best-fitting solution for the second innermost and outermost radial bins of NGC 4552, in the $\Gamma_{\rm b}$–Age (left) and $\Gamma_{\rm b}$–δTi (right) diagrams. Different line types show the impact of a number of effects, i.e. changing the modelling and fitting approach, as well as flux calibration issues (see details in Section 5), on our results. Notice that in all cases, a clear IMF radial gradient for NGC 4552 is detected. The left-hand panel shows that there is very little correlation of best-fitting Age and $\Gamma_{\rm b}$ values, i.e. our approach is able to break the Age versus IMF-slope degeneracy affecting spectral fitting at optical wavelengths alone. As seen from the black contours in the $\Gamma_{\rm b}$–δTi diagram (corresponding to the outermost radial bin of NGC 4552), the errors on $\Gamma_{\rm b}$ and δTi are significantly correlated, but the direction of this correlation is almost orthogonal to the radial variation of best-fitting $\Gamma_{\rm b}$ and δTi values. This ultimately results from the fact that the response of both TiO_1 and TiO_2 molecular features to [Ti/Fe] is comparable (Johansson et al. 2012) (i.e. $C_{\rm TiO_1} \sim C_{\rm TiO_2}$ in equation 1), while the observed radial gradient of TiO_2 in NGC 4552 is about twice that of TiO_1. It is worth noticing the strong dependence of δTi on flux calibration, as shown by the red and black contours associated with the squares in

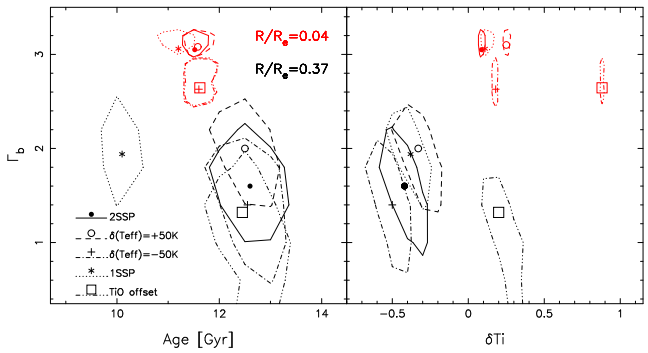

Figure C1. Probability density contours of IMF slope versus Age (left) and IMF slope versus δTi residual correction (right) for the second innermost (red) and outermost (black) radial bins of NGC 4552. The contours correspond to 1σ confidence levels. Different line styles are the results of different tests, varying the modelling/fitting approach. The contours in the left-hand panel show a mild correlated variation, illustrating how our method breaks the Age–IMF-slope degeneracy. The right-hand panel shows a correlated variation of IMF slope and δTi. However, this trend is almost orthogonal to the radial IMF-slope gradient, proving that [Ti/Fe] cannot be responsible for the observed TiO gradients.

the right-hand panel. These contours are obtained after applying an artificial shift to TiO_1 and TiO_2, mimicking a possible uncertainty on flux calibration (see Section 5). This test shows that the absolute value of δTi is not trustable, but it might be significantly affected by the reduction procedure. On the other hand, the δTi gradient is much more robust ($\Delta\delta$Ti $\sim$0.4 dex, for all different tests), and might be tracing a true radial variation of [Ti/Fe].

This paper has been typeset from a TEX/LATEX file prepared by the author.